STARS

Electronic Theses and Dissertations

2019

Design, Development, and Testing of a Miniature Fixture for Uniaxial Compression of Ceramics Coupled with In-Situ Raman Spectrometer

Ryan Jordan
University of Central Florida

STARS Citation

University of Central Florida

STARS
Showcase of Text, Archives, Research & Scholarship

DESIGN, DEVELOPMENT, AND TESTING OF A MINIATURE FIXTURE
FOR UNIAXIAL COMPRESSION OF CERAMICS COUPLED WITH *IN-SITU*
RAMAN SPECTROMETER

by

RYAN T. JORDAN
B.S. University of Central Florida, 2018

A thesis submitted in partial fulfillment of the requirements
for the degree of Master of Science
in the Department of Mechanical and Aerospace Engineering
in the College of Engineering and Computer Science
at the University of Central Florida
Orlando, Florida

Fall Term
2019

ABSTRACT

This thesis is about the design, development and integration of an in-situ compression stage which interfaces through the Leica optical microscope coupled with a Renishaw InVia micro-Raman spectrometer. This combined compression stage and Raman system will enable structural characterization of ceramics and ceramic composites. The in-situ compression stage incorporates a 440C stainless steel structural components, 6061 aluminum frame, a NEMA 23 stepper motor. Two load screws that allow to apply compressive loads up to 14,137 N, with negligible off axis loading, achieving target stresses of 500 MPa for samples of up to 6.00 mm in diameter. The system will be used in the future to study the structural changes in ceramics and ceramic composites, as well as to study thermal residual stress redistribution under applied compressive loads. A broad variety of Raman active ceramics, including the traditional structural ceramics $3mol\%Y_2O_3$-ZrO_2, B_4C, SiC, Si_3N_4, as well as exotic materials such as $LaCoO_3$ and other perovskites will be studied using this system. Calibration of the systems load cell was performed in the configured state using MTS universal testing machines. To ensure residual stresses from mounting the load cell did not invalidate the original calibration, the in-situ compression stage was tested once attached to the Renishaw Raman spectrometer using $LaCoO_3$ ceramic samples. The Raman shift of certain peaks in $LaCoO_3$ was detected indicative of the effect of the applied compressive stress on the ceramics understudy.

ACKNOWLEDGEMENTS

I would like to thank my advisor Professor Dr. Nina Orlovskaya of University of Central Florida, for her guidance and support, for her time and effort to help me learn and succeed. Performing research in design, mechanical testing, and structural characterization had allowed me to gain significant knowledge and invaluable skills. Dr. Nina has provided me with the opportunities and guidance which has allowed me to take this journey. Also, thank you to Dr. Kawai Kwok and Dr. Ranajay Ghosh for serving as my committee members.

A special thanks to my friends and colleagues, Corrina Yorke, Ruslan Kuliev, Mahmoud Omer, Dr. Anthony C. Terracciano, Tim Lindner, Clarence Bess, and everyone who shared their knowledge and expertise. The knowledge and discussion helped me better understand mechanical testing, structural characterization, design, and manufacturing, thus allowing me to succeed with my work as a researcher. Most importantly, I would like to thank my family for their love and support.

TABLE OF CONTENTS

LIST OF FIGURES

LIST OF TABLES

EQUATIONS

CHAPTER 1: INTRODUCTION

As engineers we strive to potentially find new research findings which can advance human kind. That is why this research focuses on developing means of capturing previously non-accessible aspects of material behavior under realistic operational conditions. Ceramic materials are used for a variety of energy applications including solid oxide fuel cells, turbomachinery, oxygen separation, thermal protection, armor, and cutting tools. The ceramics used in these applications sometimes operate in harsh conditions and are require to endure a multitude of mechanical stresses. Advancements in mechanical testing have provided numerous testing techniques to classify mechanical properties of current and new ceramic compositions. These tests provide characterization of instantaneous and time dependent mechanical properties of advanced ceramic and ceramic composites. Measurements of mechanical properties, such as uniaxial and biaxial strength, stress-strain deformation behavior, fracture toughness, hardness, Young's modulus, and Poisson's ratio, are important for the future design of materials and devices based on them.

Although these properties are important for proper design of components and mechanisms, and allow engineers to estimate the reliability, durability and lifetime of ceramic structures, few testing techniques allow simultaneous *in-situ* structural characterization of materials while simultaneously performing uniaxial compression testing at the same time. Therefore, the miniature compression testing device proposed in this research is of a high importance to advance the field of *in-situ* testing techniques. The miniature compression fixture will initially be used to compress cylindrical ceramics such as lanthanum cobaltite $LaCoO_3$, yttria stabilized zirconia $ZrO_3+Y_2O_3$ (ZrO_2 + 8mol% Y_2O_3 And ZrO_2 + 3mol% Y_2O_3), boron carbide B_4C, silicon nitride Si_3N_4, and silicon

carbide SiC along with many other new and unusual ceramics and ceramic composites. This thesis will aim to couple mechanical compression with structural characterization using an *in-situ* compression stage and Raman spectroscopy.

<div align="center">Efforts</div>

A compression fixture was designed as a part of the proposed testing effort and will allow for structural characterization while performing mechanical testing. This compression fixture was developed to be mounted to a Renishaw InVia Raman spectrometer for simultaneous *in-situ* mechanical and structural characterization of Raman active ceramics. The compressive stage was designed to use an electromechanical system for compression, like the systems of many modern universal testing machines. As with many other electromechanical universal testing systems, the stage has a fixed support crosshead and a moving load crosshead. A load is applied using two rotating lead screw and the applied force is measured using a load cell.

The primary reason for an in house-built compression stage is to allow the stage to be adapted to the geometry of the existing Raman spectroscopy microscope. The compression stage was designed in such a way that the microscope stage remains functionable allowing the sample being studied to still be in focus during compressive loading. In addition, microscope lenses of different magnification, and therefore size, needed to be able to reach within the required working distance of the samples surface during testing. While multiple miniature tension-compression stages are available by well know scientific companies and appear to be extremely well built with control systems which perform many of the necessary functions, these stages would not be designed specifically for integration with the existing inVia Raman spectrometer system. There have been

at least two previous attempts to design such an *in-situ* compression stage by Senior Design groups of undergraduate students. The first group tried to design and develop a very sophisticated *in-situ* compression stage that even included a self-alignment feature which would guarantee proper alignment and centric loading during uniaxial compression experiments. Unfortunately, after assembly and testing of the first stage, it was realized that the self-alignment feature caused a significant degree of eccentricity which was always present upon loading and it was not possible to apply a centric load. The lessons learned by this senior design group was well documented allowing a second Senior Design group to design a new and improved version of the compression stage. This second group only produced a preliminary improved design of a new stage before they were moved to another project; therefore, this thesis work is a last and a successful attempt to build a uniaxial compression stage.

Goals

The goal of this thesis is to develop a high-performance *in-situ* compression stage coupled with an InVia Raman spectrometer for simultaneous testing of mechanical behavior of ceramics and collection of Raman spectra of ceramics while under compression. To achieve the goal and execute the development and design of a new stage, research was broken down into the objectives as follows.

The first objective includes becoming familiar with the stages designed by past senior design students. The previous designs were thoroughly considered, and the previously designed stages' building techniques understood. The idea of the new and improved design was entertained, which includes:

3

1. Creating an improved and updated new design in SolidWorks.

2. Ensuring component tolerances are appropriate for the in-situ compression stage.

The second objective involved modelling and calculating stress at critical section of the compression fixture to verify the design was adequate. The system was verified to ensure stresses are within the allowable range for the chosen for materials and large deformations—which could cause errors in testing results—would not occur. Calculations and finite element analysis were performed in critical locations. These model and calculations included:

1. The load and support crossheads

2. The ball screws

3. The motor and transmission components

The third objective involved machining and assembling of the miniature compression stage including:

1. Manufacturing of the parts of the compression stage at the UCF machine shop.

2. Assembling all components into a functioning device.

Last, but not the least, the system was integrated with the Raman spectrometer and preliminary testing was performed to test the real-world functionality of the test fixture which will include:

1. Programing the load cell and stepper motor.

2. Attaching the compression stage to the microscope.

3. Verification and evaluation of the developed stage.
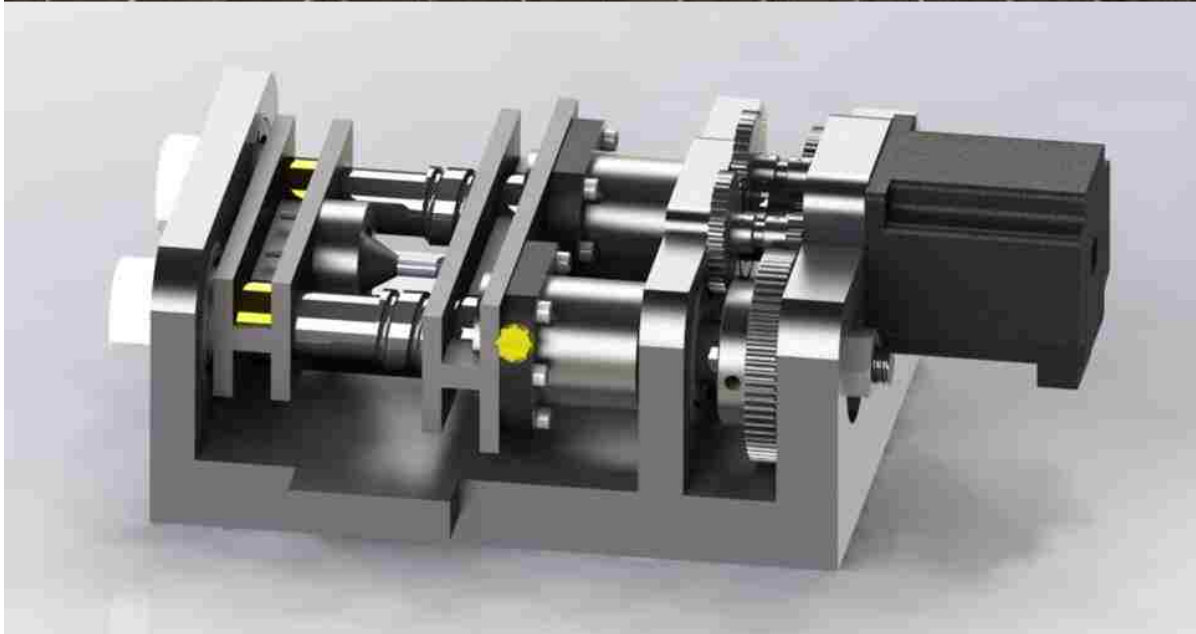
Figure 1: Render of the final compression stage design and completed compression stage.

CHAPTER 2: LITERATURE REVIEW

In order to contribute to advancing the field of ceramics forward it is important to understand the past work of other researchers. This section put the research performed by others and the research performed during this thesis into perspective. By reviewing other similar research, key concepts are defined and knowledge which helped shape the research efforts presented in subsequent chapters.

Raman Spectroscopy Overview

Spectroscopy, the study of light, involves the reflection, transmission, and scattering of light. Raman spectroscopy works by using a spectrometer which can pick up the tiny fraction of scattered light which change in wave length or color after contacting an object. This information can then be used to determine the vibrational modes of molecules.
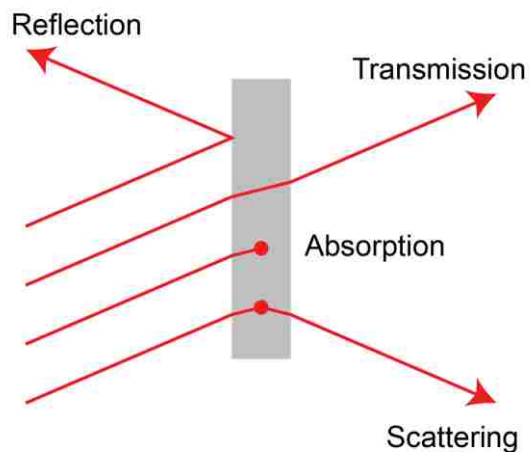
Figure 2: Fundamental photon-material interactions [1].

A small amount of reflected light, one part in 10 million, has a change in frequency because of the interaction with molecular vibrations [1]. Energy which is lost during Raman scattering is called stokes energy and energy gained in the process is called anti-stokes energy. The energy gain and loss are related to the sample's molecular vibration frequency. Measurements of the Raman spectra of Sc_2O_3-CeO_2-ZrO_2 ceramics are depicted by intensity of scattered light and frequency in figure 3.
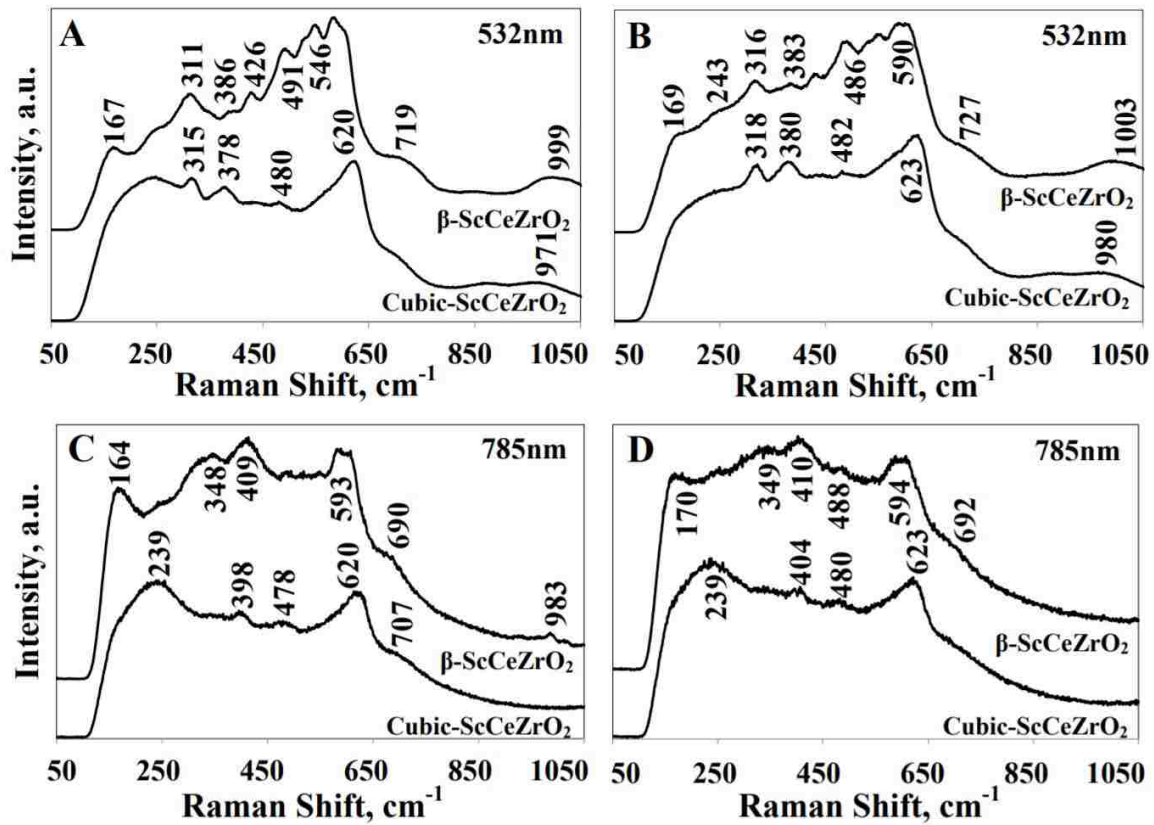
Figure 3: Vibrational spectra of cubic and rhombohedral (β) $Sc_{0.1}Ce_{0.01}ZrO_2$ ceramics;

A, C – non-deformed polished surface, B, D – center of Vickers impression [2].

Raman spectrometer systems consist of colored light sources, sometimes referred to as lasers, lenses which focus light on the sample and collect the subsequent scattered light, filters which purify the reflected and scattered light, diffraction grating or prism to split light into its constituent colors, and a detector which analysis the results. Raman spectroscopy can be used to analyze the scattered light by solid materials, such as ceramics, and characterize the materials structure. There are many advantages to Raman spectroscopy. First, structural characterization of the molecular motion of materials including ceramics can be performed without damaging the specimen. Also, many Raman spectroscopy tests have relatively easy setup procedures and short acquisition times which allows materials and components to be tested in a fast and efficient manner. The data collected during tests can then be used to provide chemical and structural information in an efficient manner [1]. It is possible other important material characteristics including residual stresses, impurities, and defects can also be uncovered. Likewise, Raman spectroscopy produces multiple challenges. One such challenge is photoluminescence, which can mask Raman information. Additional challenges include chemical glassware masking Raman signals and identifying the optimal laser power which generates significant Raman scattering without producing structural or chemical modifications to the material.

The specific Raman spectroscopy system, which is used to be coupled with the proposed compression stage is the Renishaw InVia Raman spectroscope (Wotton-under-Edge, United Kingdom). The Leica DMLM optical microscope is to be used as a base for the compression stage attached to it. It will also allow focusing of the ceramic sample by adjusting the compression fixture in the Z-direction. While performing Raman spectral acquisitions, a 532nm silicon laser with a maximum power of 100mW is used to excite the ceramic samples. Long working distance

objective lenses will be used focus on the sample and include Olympus SLMPLN50X and Olympus LMPLFLN20X lenses.
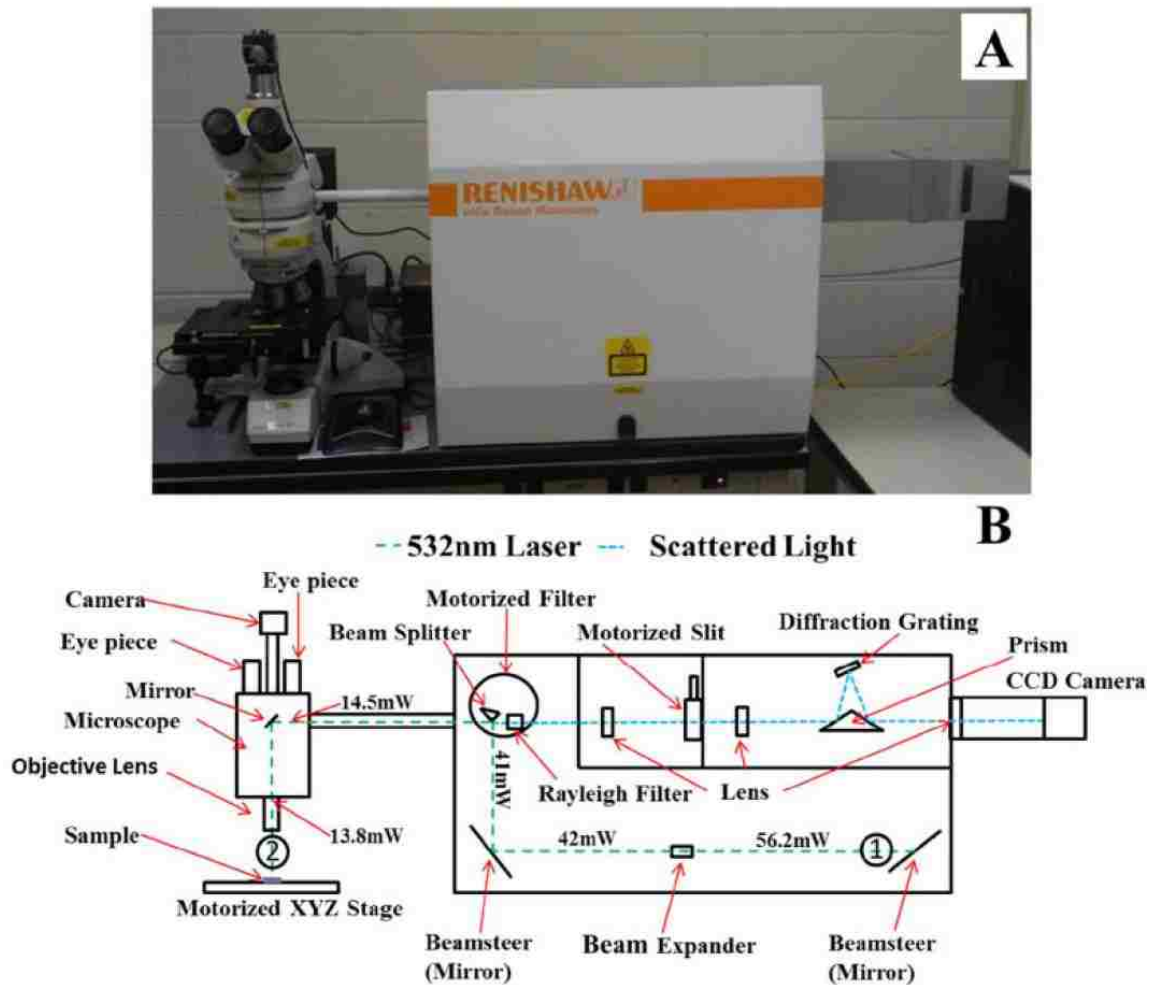
Figure 4: (A) Raman InVia spectrometer and (B) schematic of spectrometer [3].

Ceramics Material Overview

This chapter focuses on the materials properties and Raman responses of ceramics which have been used and will be tested using the miniature compression fixture. The first tested using the

compression fixture was lanthanum cobaltite ($LaCoO_3$). Other materials, such as yttria stabilized zirconia ($ZrO_3+Y_2O_3$), boron carbide (B_4C), Silicon Nitride (Si_3N_4), and Silicon Carbide (SiC), will be tested using the developed stage in the future research work.

$LaCoO_3$ is a perovskite with a rhombohedral crystal structure. This material has been shown to exhibit ferroelastic behavior, which was attributed to domain switching under stress application [4]. Lanthanum cobaltite uses include cathodes in oxides for solid oxide fuel cells, exhaust gas sensors in automobiles, catalysts, and membranes for oxygen separation and permeation processes [5] [6]. In the past, micro-Raman spectroscopy has been used to study $LaCoO_3$ to evaluate the appearance of the residual surface tensile or compressive stresses induced during Vickers indentation testing [7].
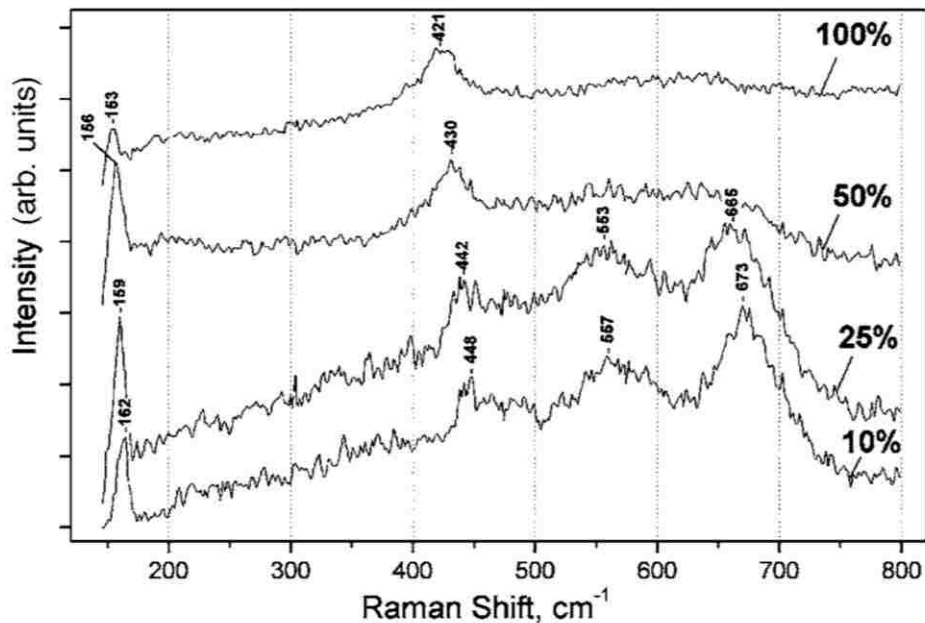
Figure 5: Raman scattering of $LaCoO_3$ perovskite at different laser intensities [7].

10
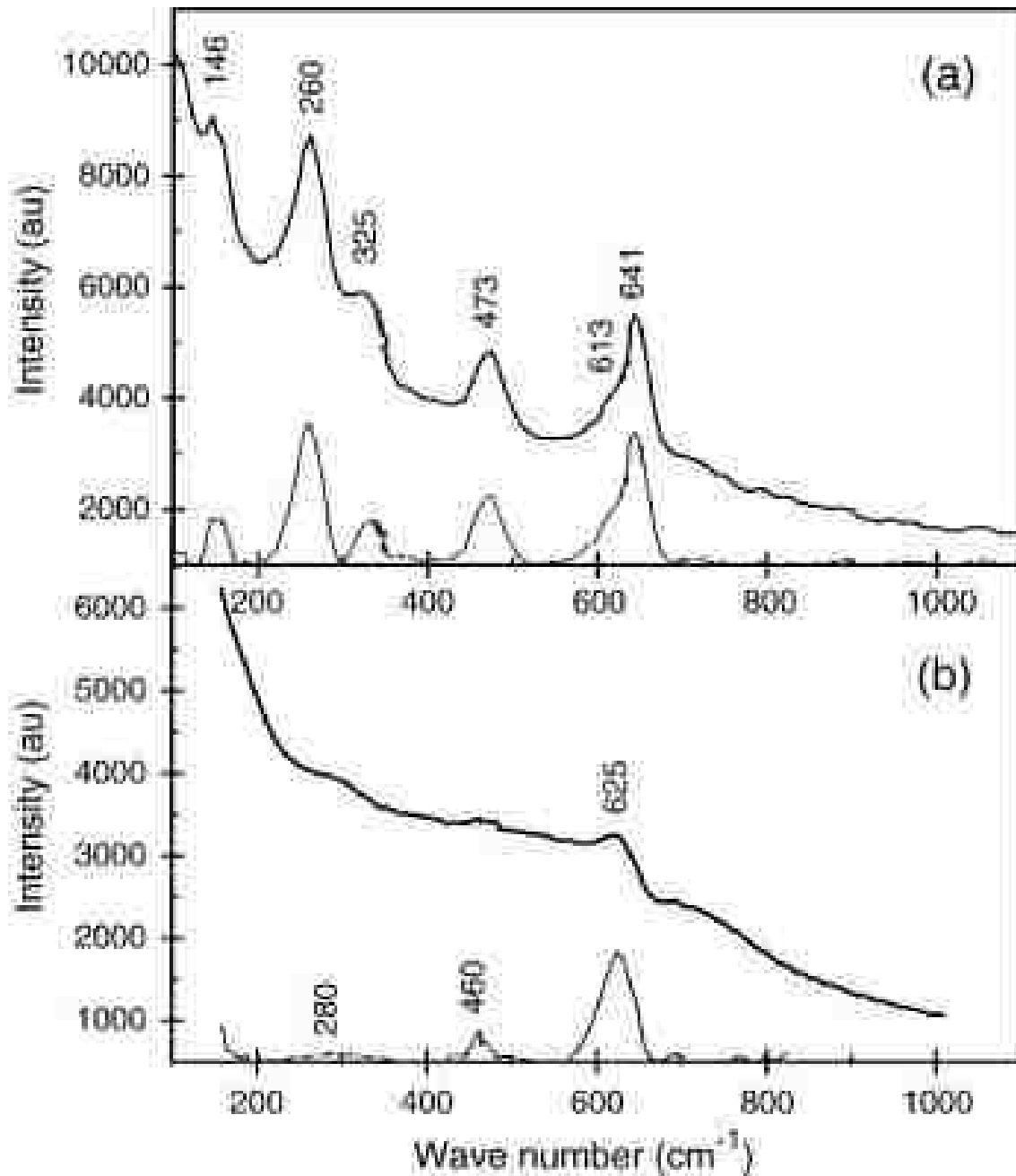
Figure 6: Spectra of sintered (a) 3Y-TZP and (b) 8Y-FSZ. Solid line for original and dashed line for background subtracted spectrum [9].

Yttria stabilized zirconia with compositions of 3 mol% Y_2O_3-stabilized tetragonal zirconia polycrystals (3Y-TZPs) and 8 mol% Y_2O_3-stabilized cubic zirconia (8Y-CSZ) are an important

class of ceramic materials because of either transformation toughening occurring in 3Y-TZP or fast ionic conduction occurring in 8Y-CSZ [8] [9]. Uses of yittria stabilized zirconia include electrode materials in solid oxide fuel cells and oxygen separation membranes. Yttria stabilized zirconia has been studied in the past uses Raman spectroscopy and its typical spectra (figure 6).

Boron carbide is a ceramic with a rhombohedral crystal structure which has a low theoretical density and high hardness [10] [11]. Examples of uses for boron carbide include armor because of its low density and high hardness and absorption of neutron for nuclear reactors because of its high neutron cross section for absorption [11]. In the past, Raman spectroscopy has been used to evaluate the micro-structure structure of boron carbide (figure 7).
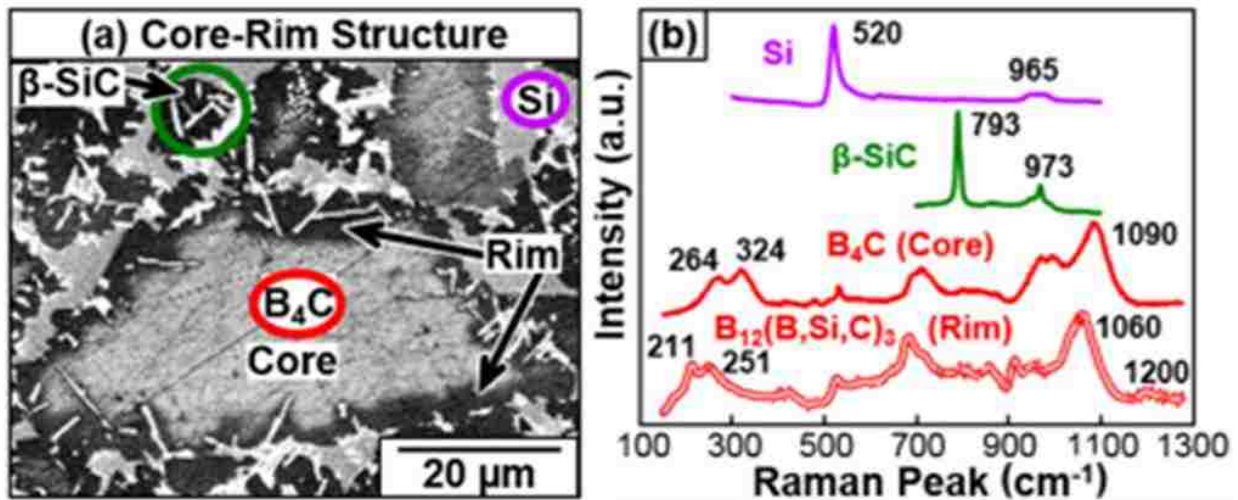
Figure 7: (a) Secondary electron image of a reaction bonded B$_4$C microstructure revealing a core-rim structure (b) Raman spectra for the phases present: Si, SiC, B$_4$C (core), and (B,Si,C) (rim) [12].

Silicon nitride has a cubic or hexagonal crystal structure and is used for cutting tools and high temperature applications such as rocket thrusters [13] [14] [15]. In the past, structural characterization of cubic silicon nitride has been performed using Raman spectroscopy (Figure 8).
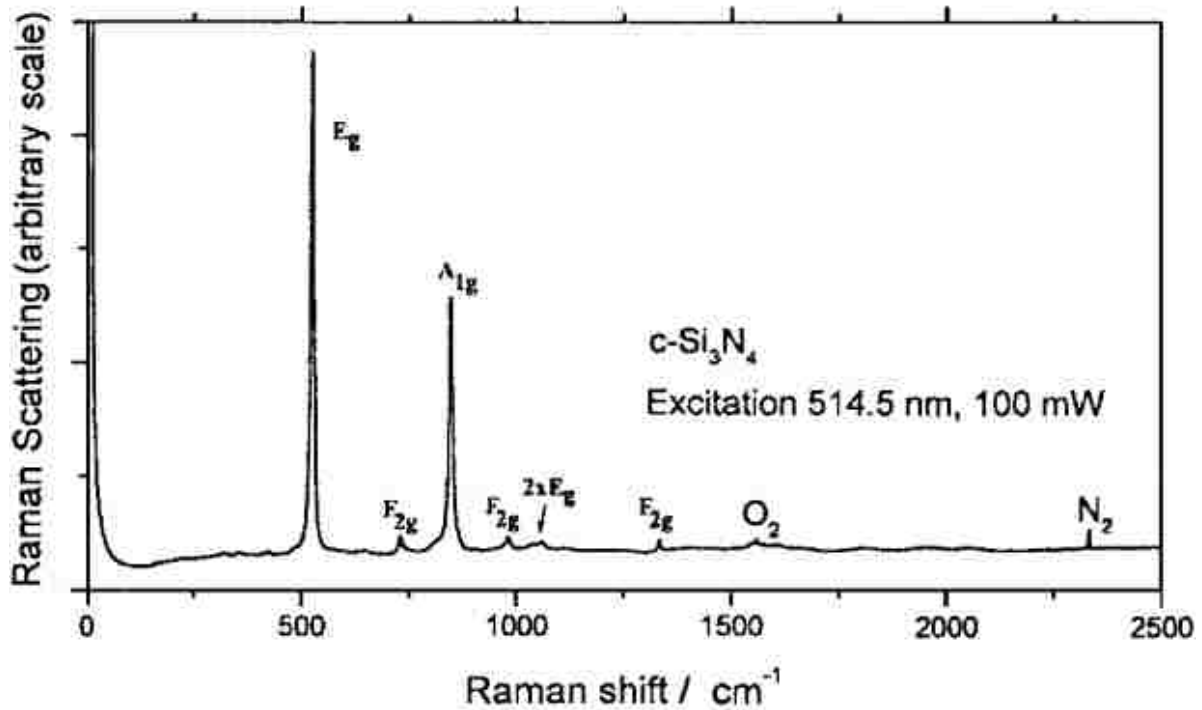
Figure 8: A typical Raman spectrum for the cubic spinel Si3N4 phase measured with 514.5 nm excitation at 295 K [16].

Silicon carbide is known to have a wide variety of poly types including cubic, hexagonal, and rhombohedral crystalline structures [17]. Uses of silicon carbide include armor, cutting tools, and thermal protection systems for space applications [18] [19]. Structural investigation of silicon carbide has also been performed in the past using micro-Raman spectroscopy (figure 9).
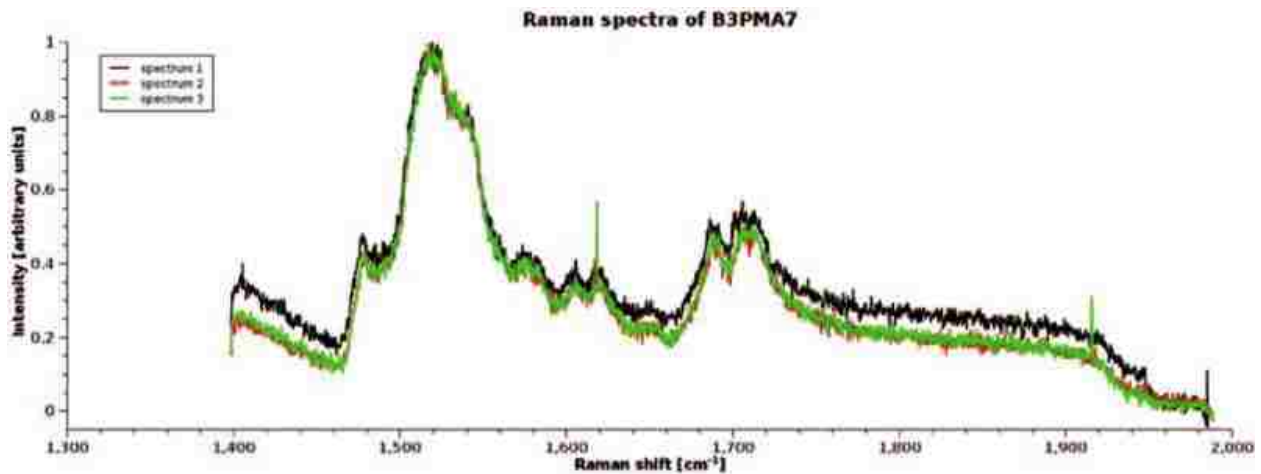
Figure 9: Comparison the of Raman spectra of 4H-SiC (B3PMA7) measured for different z

positions [20].

In-situ Mechanical Testing and Structural Characterization

In the past, researchers have made great progress coupling mechanical testing with structural characterization. The studies reviewed in this section use different mechanical testing techniques, structural characterization methods, and materials which demonstrates the importance of mechanical testing while performing structural characterization in a multitude of research areas. Key research projects were reviewed to understand conceptually similar studies and to put the work of this thesis into perspective.

Nanomechanical testing was performed on Ni nanopillars using a Pico indenter equipped with a diamond flat-tipped punch tip [21]. This Bruker Hysteron PI 95 TEM picoindenter (Bruker, Billerica, MA) was used to perform unique loads by loading individual nanostructures while viewing the experiment using a transmission electron microscope.

Figure 10: Hysteron PI 95 TEM Pico indenter with close of loading tip [22].

In the past using traditional testing methods, the inability to see deformation of nanoparticles has been a major obstacle while determining mechanical properties. This problem was addressed by using a transmission electron microscope to simultaneously view the individual nanostructure while compressive forces were induced.
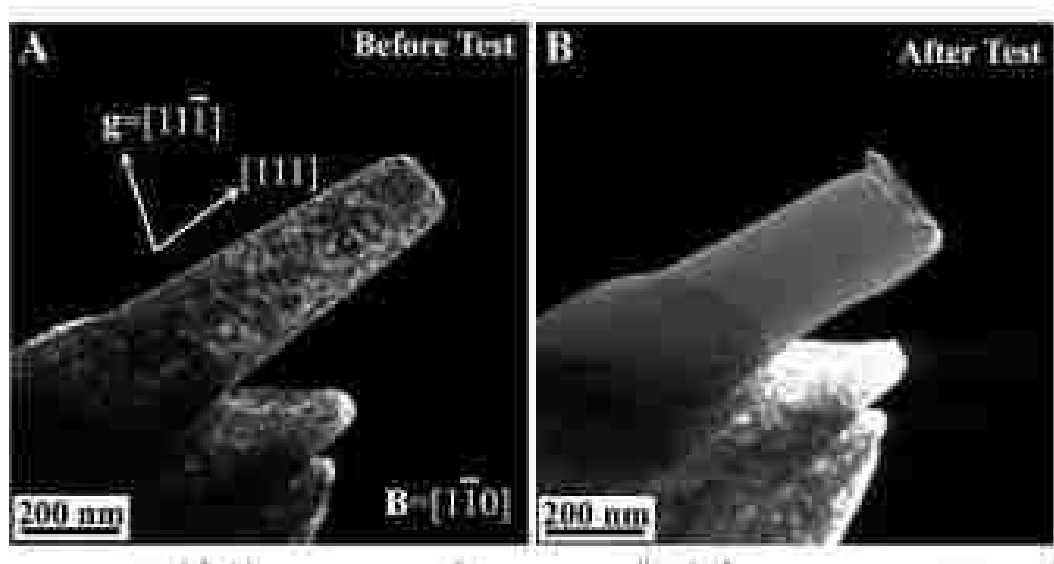
Figure 11: (A) Dark-field TEM image of Ni nanopillar before compression, (B) and after compression [21].

High strength is exhibited by many nanoscale materials and this research helped to provide insight into the mechanisms which are involved with this phenomenon. It was observed that upon contact

15

with the picoindentor, the nanopillars yielded and as increased compressive strain was introduced, pre-existing defects disappeared resulting in essentially a dislocation free single crystal. This required large increases in compressive load to induce elastic behavior in the specimen. Individual frames recorder by the TEM allowed the instantaneous contact area to be measured. Large fluctuation was observed in the force vs. time graph of the experiment likely due to mechanical annealing, which created a stronger structure [21]. The data provide greater understanding into the phenomena responsible for the strain hardening or mechanical annealing observed in nanostructures.

In another journal article researchers developed and tested an *in-situ* three-point bending device which can induce a constant bending stress while performing micro-Raman measurements to measure the vibrational responses of different ceramic materials such as ZrB_2-SiC particulate ceramic composites [23]. The three-point bending devise was design for samples with dimensions between 3 mm x 4 mm x 45 mm and 2 mm x 2.5 mm x 35 mm and could induce a maximum load of 70 N resulting in a maximum stress of 100-360 MPa depending on sample size. Operation of the three-point bending devise is controlled via a stepper motor which drives two worm gears. The gear reduction created by the worm gears allows the devise to achieve higher torque and a lower loading rate. Circular motion is finally translated into linear displacement via parallel lead screws. A load cell is used to measure the mechanical force applied by the three-point bending test.

Material characterization was performed using a commercially available Raman spectrometer with a 532 nm light source and holographic notch filters. Both the Raman spectrometer and the three-point bending devise were calibrated prior to collecting data. First, the spectrometer was calibrated with calibrated with a Si standard using a Si peak position at $520*3$ cm^{-1}.
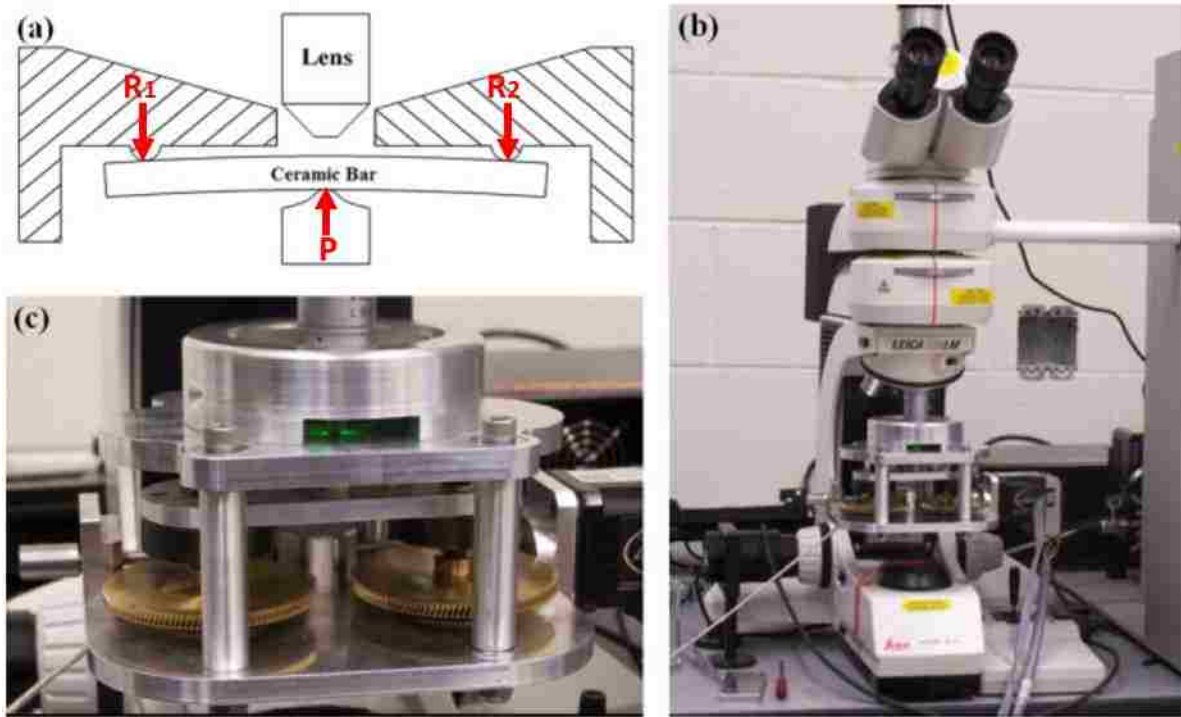
Figure 12: (a) schematic of loading ceramic bar in three point bending for collection of in situ scattered light, (b) photograph of in situ loading device and (c) loading device coupled with Leica optical microscope connected to InVia microRaman spectrometer [23].

The three-point bending fixtures load cell was calibrated by applying weights ranging from 10 to 200 grams to the screw platform while the corresponding voltage was recorded. Then using materials with a known Youngs modulus, aluminum 2024 T3, the accuracy of the bending devise was checked by using an attached strain gage. Each sample was loaded and unloaded 5 times and the stress strain curves were collected.
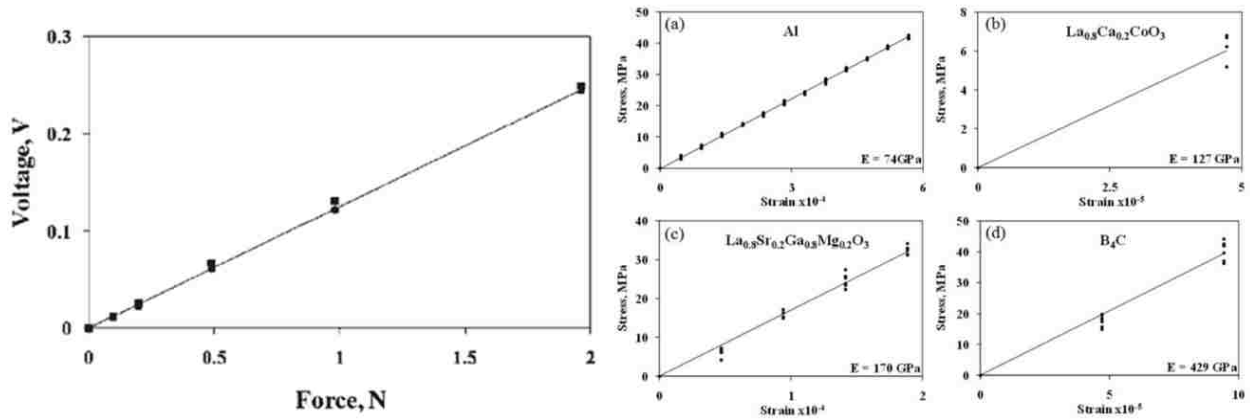
Figure 13: Force applied versus voltage output for calibration of load cell and stress-strain

deformation curves obtained by loading samples in the in situ loading device [23].

Finally, after the initial setup was performed, the dependence of peak position and stress could be tested using in-situ three-point bending devise. SiC bands are sensitive to stress changes, therefore, Raman peak intensities of SiC were used to study the effects of a bending load on the ZrB_2 + 10wt%SiC ceramic material. After placing the samples in the devise without a load, the spectra of the samples were calculated. Next, the spectrums were collected at multiple different loads ranging from 12.5 to 75 MPa. One peak was used to study because other peaks exhibited overlapping. All peak shifts transitioned to a lower wave number as bending stress was applied because of the tensile stress present in the material. Both linear and quadratic fits were performed and a relationship between peak position and applied stress was developed.
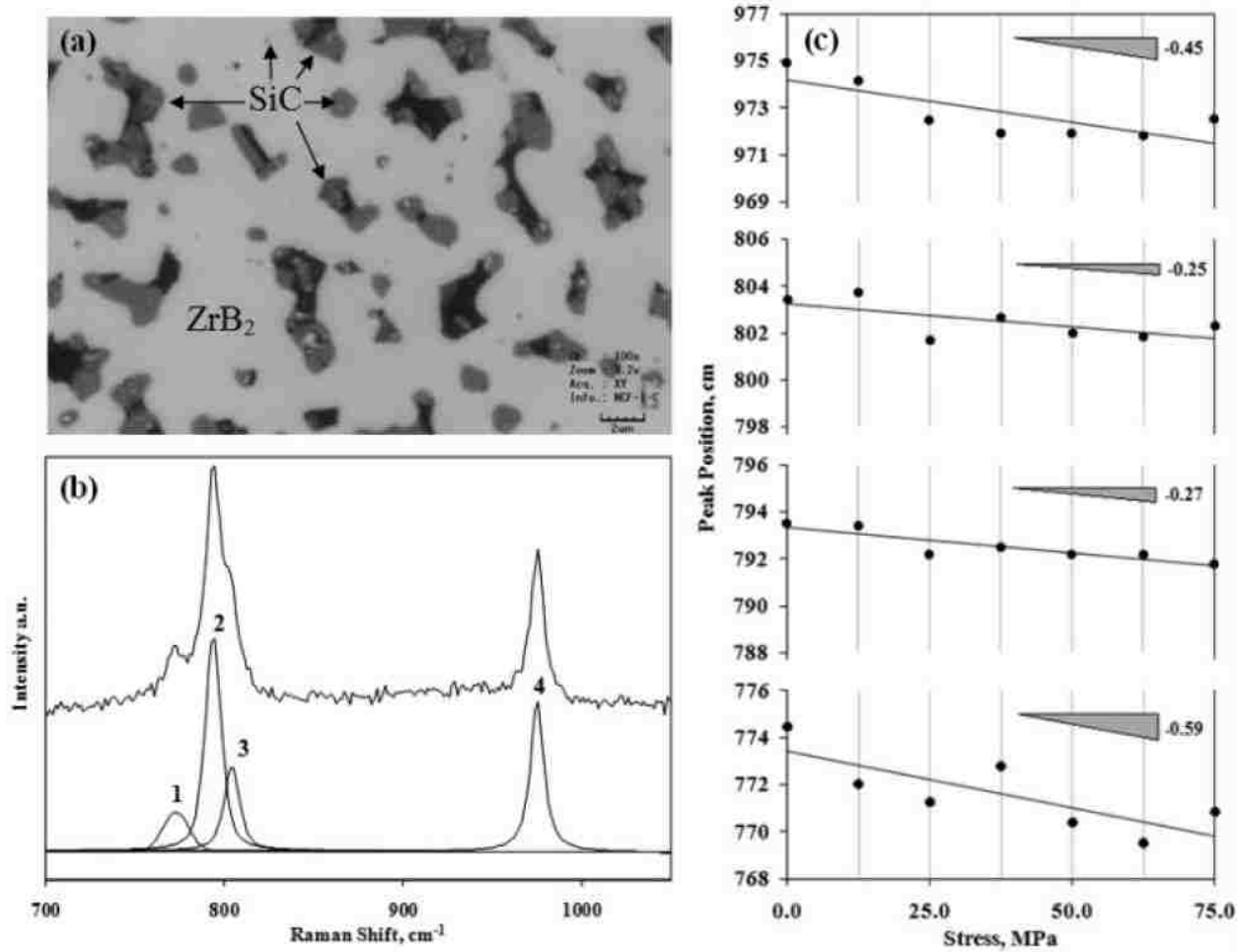
Figure 14: (A) Optical micrograph of ZrB$_2$+10wt%SiC ceramic composite. (B) Raman spectrograph of 6H-SiC phase in ZrB2-10 wt-%SiC ceramic composites: peaks numbered 1, 2 and 3 are modes of 6H-SiC and peak 4 is LO mode of 6H-SiC. (C) applied stress dependence of peak position of transverse optical and LO modes of 6H-SiC ceramics [23].

Raman mapping of ZrB$_2$–SiC ceramic composites was performed by researchers using a commercially available Renishaw inVia micro-Raman spectrometer to perform micro stress analysis on ceramics [3]. Micro stress is caused by thermal residual stresses from sintering and has a significant effect on the material properties of ceramics. Using this technique, it is possible to

determine micro stresses within the ceramic sample by using the relationship between residual micro-stresses and Raman band frequencies. This paper explores the ideal parameters such as collection time, laser power, type of scan, and step resolution to produce micro-Raman spectrometer maps.
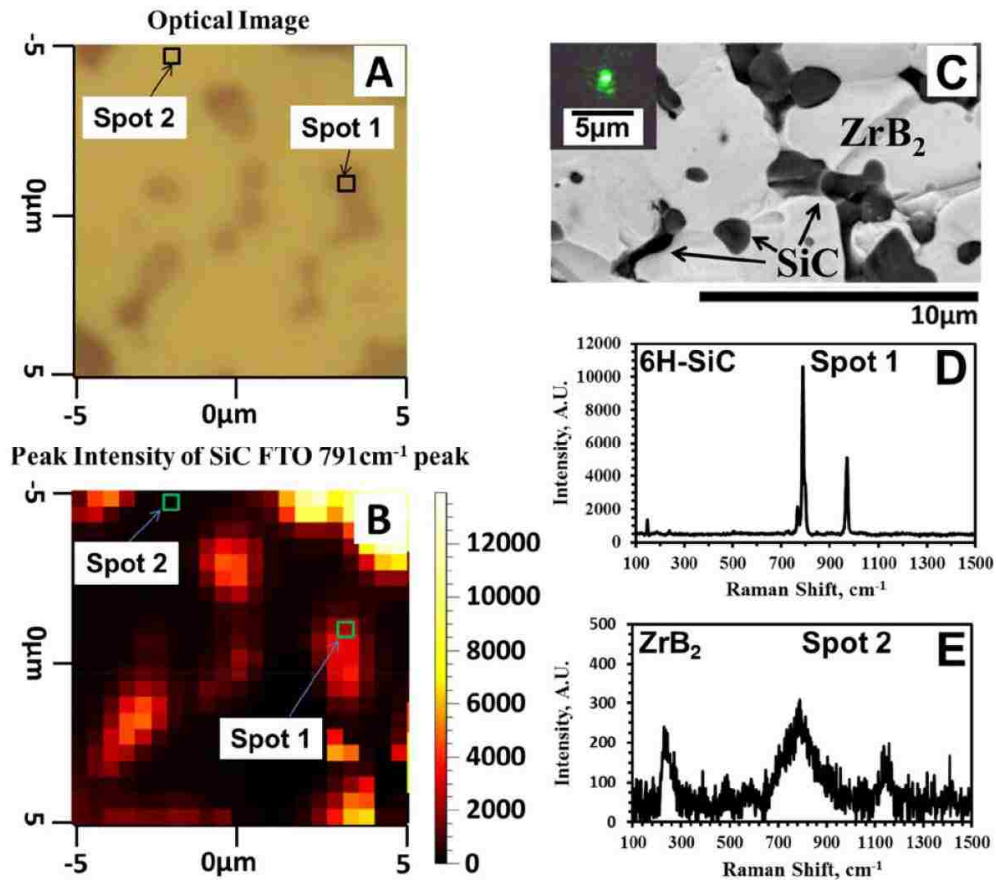
Figure 15: (A) Optical image of ZrB_2–SiC ceramic , (B)Spectrometer map, (C) SEM backscattered image of ZrB_2-10 wt-% SiC, inset shows laser spot size taken using 6100 objective lens, (D) typical Raman spectra for SiC phase spot 1 of Spectrometer Map, and (E) typical Raman spectra for ZrB2 phase spot 2 of Spectrometer map [3].

The best set points for exposure time and scan type were determined for ZrB_2-10wt-%SiC. It was determined by the researchers that an exposure time of 30 seconds and a static or scan with a resolution of 0.5 um produced the highest quality results.

In-situ compression of submicron structures and particles in a high-resolution SEM was performed by researchers after developing a device for *in-situ* compression which was coupled with a scanning electron microscope [24]. Measuring mechanical properties of nanoparticulate can be very difficult and currently there is no analytical approach or solution for complex stress fields in small particles. Therefore, experimentsal testing is the only way to characterize particle systems directly. Previous measurement techniques such as indention test create complex stress fields during loading. To solve problems of other tests, a more intuitive way was needed and little work has been performed working with compression of submicro sized particles. To solve this problem, the authors believed uniaxial loading of small structures using simple geometries in a scanning electron microscope (SEM) field would be adequate. Advantages of SEM include very high working distance, larger space, and easy sample preparation when compared to transmission electron microscopy. Likewise, one disadvantage is measurements are limited to regions near the surface. Advances made in the field of micromechanics and electron microscopy also make using this technology in conjuction with uniaxial loading possible.
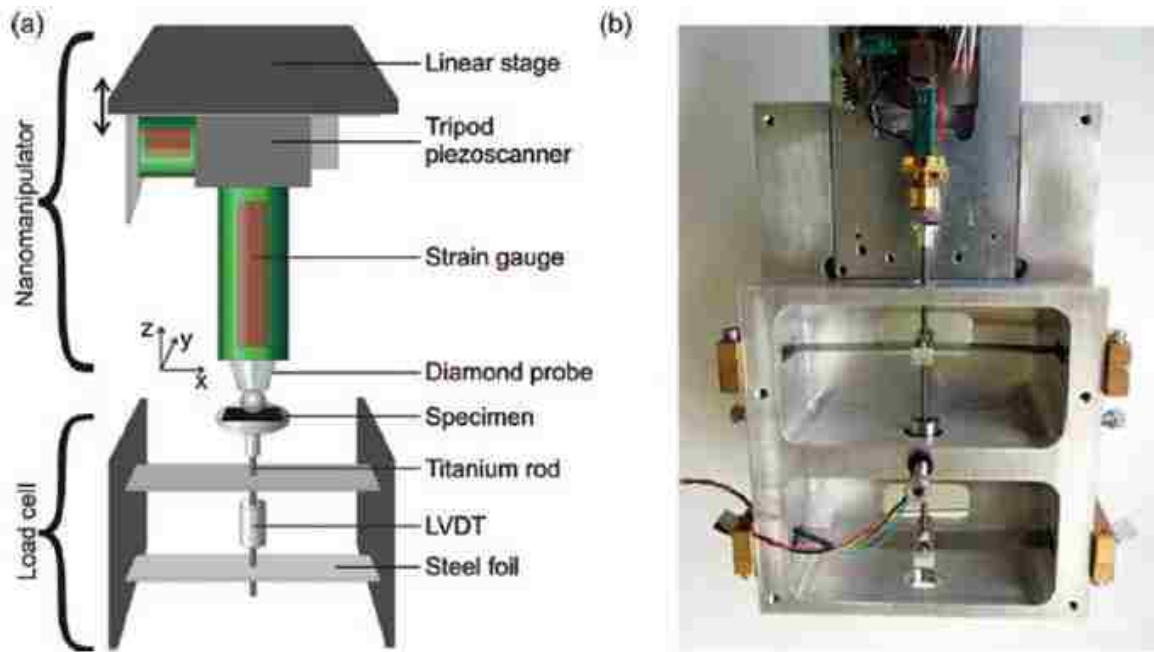
Figure 16: Schematic diagram (a) and a photographic image (b) of the in situ [24].

The compression device apparatus consisted of two main assemblies which are described as the upper and lower parts. The upper part carries out all movements and the lower part contains the load cell and sample support. The compression device is made from multiple materials. First the carrying frame is completely made from a standard aluminum alloy and steel spring with different spring constants were using for loading. Additonal materials used in the design included titiamium, brass and vacuum compatible polymers. One design challenge was making sure the device could fit inside the vacuum chanber of the SEM machine. Movement control of the system is performed using a closed loop piezoelectric tripod scanner and screw driven style stage. Course adjustment is provided via the stage. Via the stage, while fine adjustment is controlled via piezoelectric tripod scanner. The compression of the devise is controlled by a simple system which is comprised of interlocking steel foils, clamping jaws, and a titanium rod. This can produce a load from a spring

22

constant ranging from 30 N/m to 50000 N/m. Tension of the interlocked steel foils is adjusted by changing the relative positions of the clamping jaws on the titanium rod. Changing the spring constant of the load cell leads results in a change of force resolution. For calibration, the spring constant is determined prior to each experiment by moving the sample stage slightly and relating this to the masses and Eigen frequencies of the system.
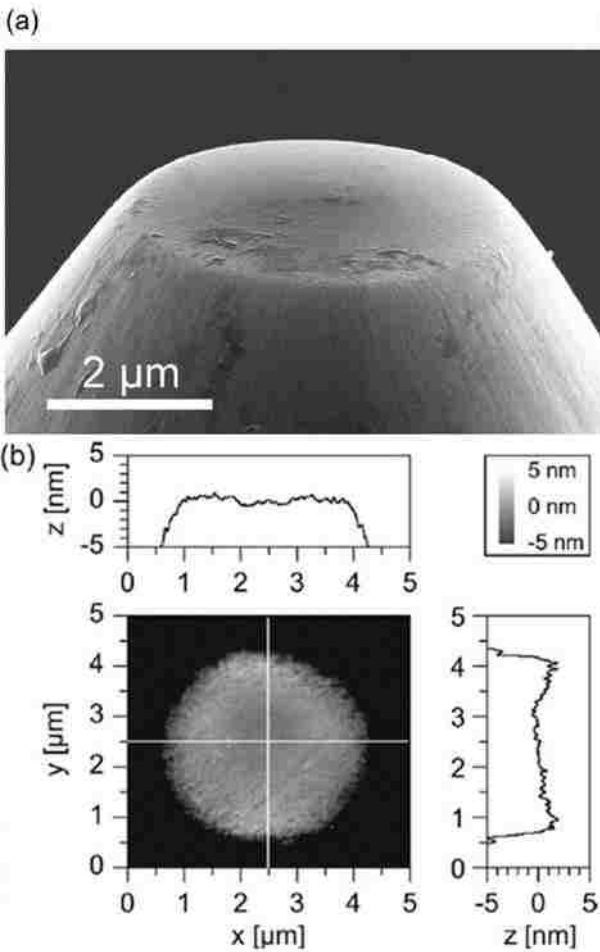
Figure 17: SEM image of the used diamond flat punch indenter (a) accompanied by an AFM image (b) characterizing the rms roughness of the plateau [24].

A unique set of equations are used to processes the data which is recorded by the researchers. Force and deformation data are determined from the probe's movement normal to the samples surface which is measured via a stain gage. The loading force normal to the samples is determined using the spring deflection related with the LVDT output voltage and the spring constant which is calculated using the equation 1.

Equation 1: Load force normal to sample.

$$F = D\frac{\Delta U_m}{\sigma} \tag{1}$$

The sample deformation is also calculated using equation 2.

Equation 2: Sample deformation.

$$\delta_t = (\Delta Z_m - \zeta) - \frac{\Delta U_m}{\sigma} \tag{2}$$

The mechanical behavior of in-situ chondrocytes under compression was studied using an *in-situ* compression system in conjunction with a laser scanning microscope to investigate the effects of cartilage tissue lesions [25].
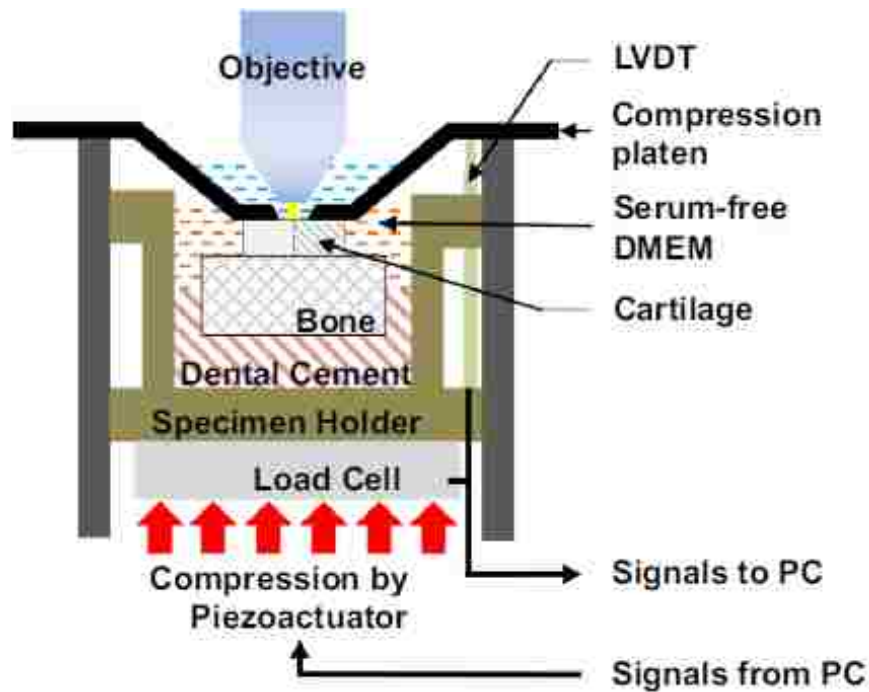
Figure 18: Schematic illustration of the in-situ compression system. The chondral block was compressed against a light-transmissible platen by a piezo-actuator. The vertical displacement was monitored by a displacement transducer [25].

Collagen fibers and proteoglycans provide tensile and compressive strength to joints. Chondrocytes are the healthy cells found in cartilage, were as, Lesions are areas of tissue which have suffered damage. Experimental and numerical approaches were used in this study to investigate the effects of cartilage tissue lesions on the mechanical behavior on *in-situ* chondrocytes. A loading fixture which was light-transmissible was designed and mounted onto the stage of a laser scanning microscope.

In the experiment the tissue was compressed to 15% nominal stain. Also, a control set of tissue was not compressed. The data obtained using dual photo excitation microscopy was expressed using statistical analysis including the mean and standard error. The finite element model was

based off a pre-established two-scale model which had previously been used to study in-situ mechanical behavior of chondrocytes.
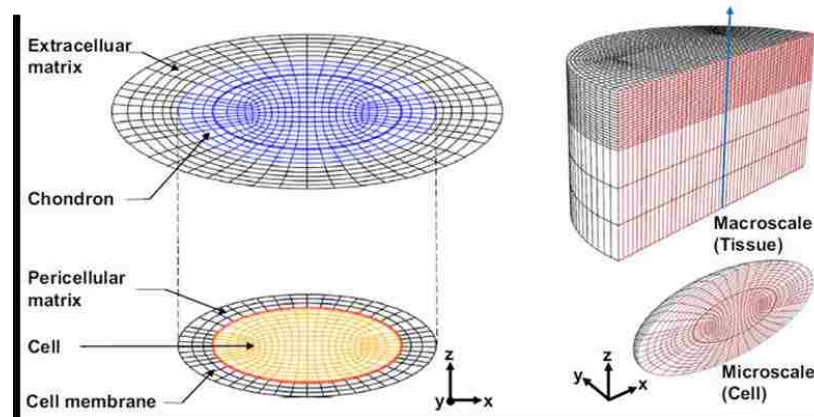
Figure 19: Articular cartilage tissue and chondron mesh models [25].

The cartilage and bone joints were modelled two separate ways. First, tissue level or macroscale model was created. Then, a cell level or microscale model was created. Material properties of the macroscale property were assumed to be dependent on tissue thickness. The cartilage was assumed to be non-homogeneous and non-linear. The bone was modelled as biphasic, homogeneous and linear. The FE package used was Abaqus v6.12 and a 3D model was utilized. Deformation caused by compression during the physical test was displayed in the results, along with the results of the finite element analysis. Results of the compression test were recorded during three-time points and five normalized radial locations. Shear stress, axial strains, and fluid flow were recorded. The author noted that lesions experienced higher fluid flow and small tensile stresses while intact tissue experienced large axial compressive strains. Higher shear strain was also located near tissue lesions [25]. It was expected that the lesions tissue would deform more than intact tissue, but the opposite was found for the steady state conditions. A second experiment was also performed for

26

multiple compression-recovery cycles. When the samples were compressed multiple times, the cells deformed less each time due to residual deformation. Actual cell mechanics were more closely represented by the second test were smaller repeated cycles were performed.

The numerical results also confirmed the experimental results. The FE model of cells was analyzed using the best-fit ellipsoid approach and four-point marker approach [25]. The best-fit ellipsoid approach was found to be unsatisfactory to estimate cell shear because of rigid body rotation. The four-point marker technique was successful for estimating the Green-Lagrange strain tensor [25]. The studies conducted in this research provide crucial insight to the mechanical response of lesioned joints and although more research needs to be performed, important findings were determined about the steady state and transition phase mechanics of the joints.
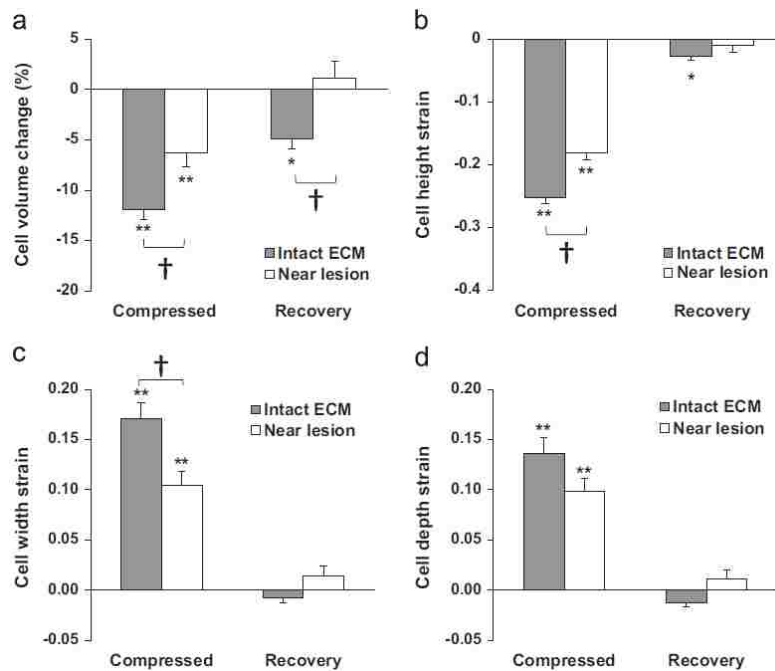
Figure 20: Changes in cell morphology in the intact ECM or near tissue lesions during the tissue compression phase and the recovery phase [25].

Other devices for in-situ testing of the mechanical properties of materials were developed and the results of their testing are presented in [26] [27] [28].

Micro Mechanical Testing Devises

In addition to the home made in-situ stages, commercially available micromechanical testing devices are also available [29] [30] [31]. A brief overview is presented below and are based off the manufacturer website, specification sheets, and documentation. Also, journal articles or reports which use these devices are mentioned.

The Kammrath and weiss tensile and compression module (figure 21) [29]. This micro tensile and compression test device is design for dynamic and static testing for use with scanning electron microscopes (SEM). This devise can perform cyclic testing and has a load range of 10uN to 5000N. This in-situ compression devise was used while performing EBSD analyses in Bunker application note #EBSD-02 [32].
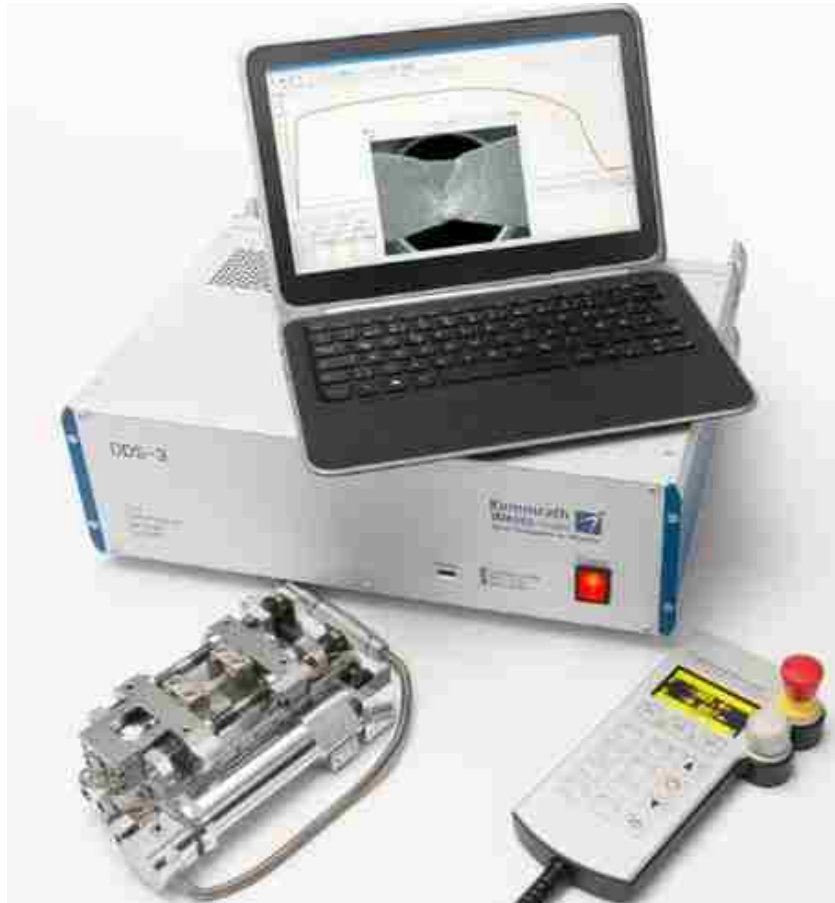
Figure 21: The Kammrath and weiss tensile and compression module [29].

Another high quality commercially available compression tester is the MTI instruments SEM series tensile Tester [30]. This stage is built for LM, SEM, and XRD structural testing. It can be used for tensile, compression, and cyclic testing. In this design the way the grips clamp the sample would not work for ceramic samples because of their brittle nature. The manufacturer offers multiple designs which have load frames with capacities between 450N and 9000N.
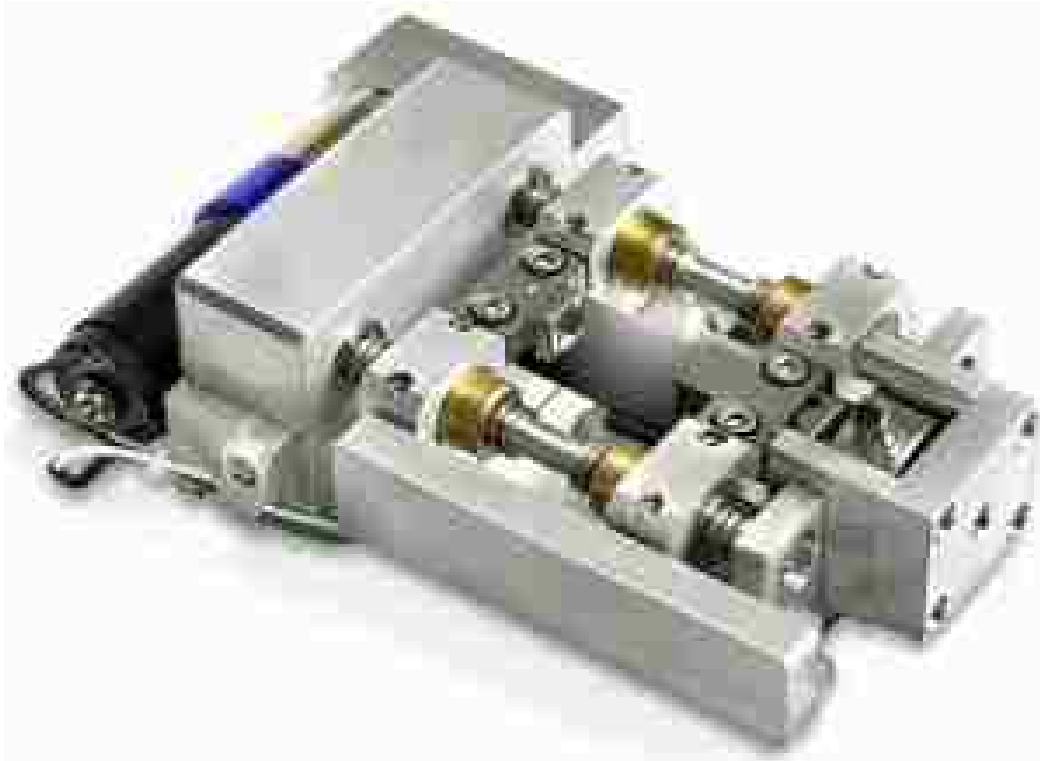
Figure 22: MTI instruments SEM series tensile Tester [30].

Finally, there is Deben compression & horizontal bending stage available on the market [31]. According to the manufacturer, this system is design for use with SEM, optical microscope, AFM or XRD system. This stage offers load cells from 2N to 200N and has multiple clamping options for three-point bending, four-point bending, tensile, and compression.

Figure 23: Deben compression & horizontal bending stage [31].

Senior Design Compression Stages

In the past, at least two, University of Central Florida, senior design groups have design or developed compression stages with an intent to be used for *in-situ* Raman spectroscopy. The first Senior Design group successfully completed a working compression stage and performed testing on ceramic samples (figure 24). Unfortunately, a mechanism on the load crosshead which was designed to prevent eccentric loading by self-aligning the sample did not properly function and instead created eccentric loads. Also, to save weight, undersized ball screws were used in the student's design. Nevertheless, Senior Design students' stage had an outstanding design with a complex assembly which provided multiple lesson learned from their attempt. Lessons learned included the necessary use of properly sized ball screw, challenges with sample alignment, the importance of using materials which minimize deflections, and choosing a design which minimizes machining time. In the new design larger lead screws and ball nuts were used which were rated for

31

the required higher loads. Also, a larger gear reduction was implemented using a two-stage transmission to increase torque. The original sample alignment fixture was removed, and instead precise machining was used to ensure the sample under compression is well aligned and a compressive load was applied centrically. To minimize deflections, the load path is constrained between the 440C stainless steel crossheads and the ball screw system instead of the aluminum body.

Figure 24: First compression stage designed produced by UCF senior design team.

The second Senior Design group designed a new compression (figure 25) but was unable to complete the design due to their project being reassigned after the first semester. This second design also had some great feature which were included in the latest design presented in this thesis. These features include a modular aluminum stage frame which allows the stage frame to be machined out of four components requiring less material removal. It also includes I-beam style load and support crossheads which increase the moment of inertia, therefore decreasing crosshead

deflection, minimizing eccentric loading, and saving weight. A smaller and lighter stepper motor

was also able to be used due to the large gear reduction.
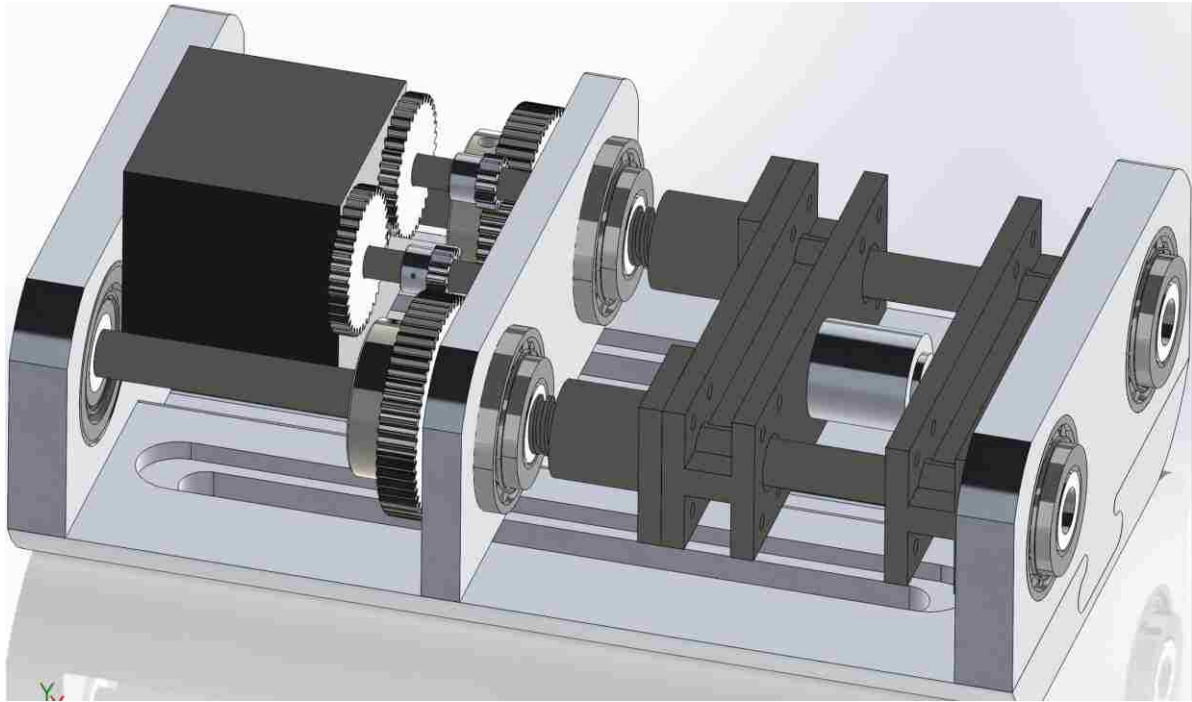
Figure 25: Second design of the compression stage which will be a basis of the redesign.

CHAPTER 3: DESIGN

A miniature *in-situ* compression fixture was designed to be mounted on a Leica optical microscope and to be used to perform *in-situ* structural-mechanical testing in conjunction with an InVia micro-Raman spectrometer. The design and calculations of the compression fixture are displayed in this section and include: the design criteria, important system analytical calculations, the design in CAD, finite element analysis, and design of the control system.

Design criteria

The micro compression fixture was designed with the ability to compress cylindrical ceramic specimen up to 12 mm in length and with a diameter up to 6 mm. The electrical mechanical loading system was designed to produce a load up to 14137 N in compression. The desired maximum compressive stress samples with a diameter of 6.00 mm of 500 MPa. It is also important that the load fixture is rigid, and the load and support platens which contact the specimen being tested must remain parallel to prevent eccentric loading. In the future, the simple design of the loading fixture could allow for samples of other geometries such as rectangular samples to be tested. Although the compression fixture was initially designed for cylindrical samples of 2.00 mm in diameter x 4.00 mm in height and 6.00 mm in diameter x 12.00 mm height, the fixture was designed with the intent that samples with similar geometries could be tested with minor modification. The use of samples with different dimensions would require platens that accommodate the cross-sectional area and they would need to fit within the load and the support fixture.

Figure 26: LaCoO$_3$ cylindrical ceramic sample used for testing with a diameter of 6.04mm.

In order to perform mechanical testing and structural characterization, the stage was combined with a Leica DMLM optical microscope which focuses the light of the Raman InVia spectrometer via objective lenses of specified magnifications and working distances. Designing the compression stage to connect to the optical microscope posted its own set of challenges. Challenges included keeping the compression stage small enough to fit in the microscope stage area, the weight of the compression stage, and allowing adequate room for the Leica 50x lenses to focus on the samples.
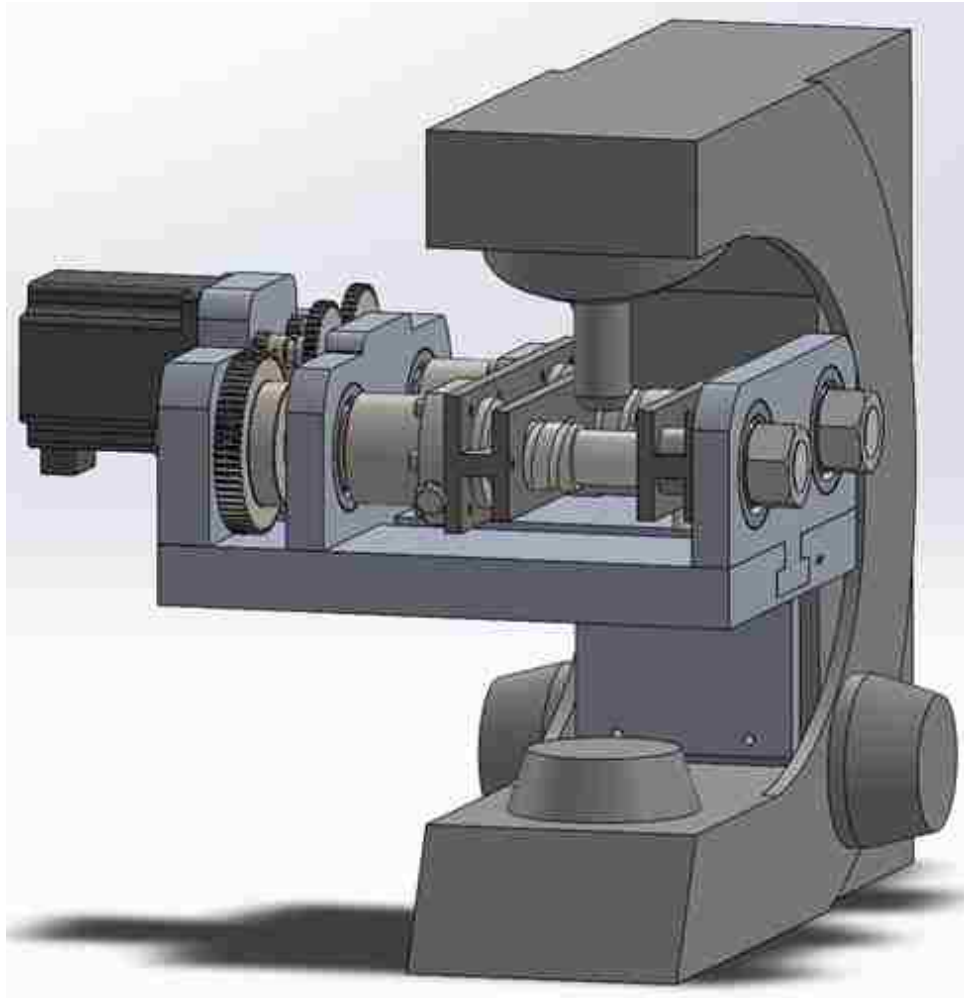
Figure 27: Leica DMLM microscope with compression fixture attached and CAD model of

microscope.

In order to use the microscopes stage alignment mounting points, it was necessary to ensure the

weight of the compression stage was minimized to mitigate significant misalignment or damage

to the microscope's components. Although Leica was unable to provide an exact weight

requirement of their microscope, a representative of the company suggested keeping the load the

microscope encountered under 4.5Kg to avoid damage. Therefore, early in the design process it

was determined that the stage needed to be under 4.5 kg or a mechanism which supports the microscope to reduce the strain induced on the focusing components needed to be developed.

The design was also required to allow the microscope to focus on the sample. Because different magnification lenses have different diameters, lengths, and working distances these criteria proved to be challenging. In figure 28 the photograph of different sizes of magnification lenses (Figure 30A-D) and an example of the 50x long working distance lenses fit check in SolidWorks are also presented (Figure 30F).
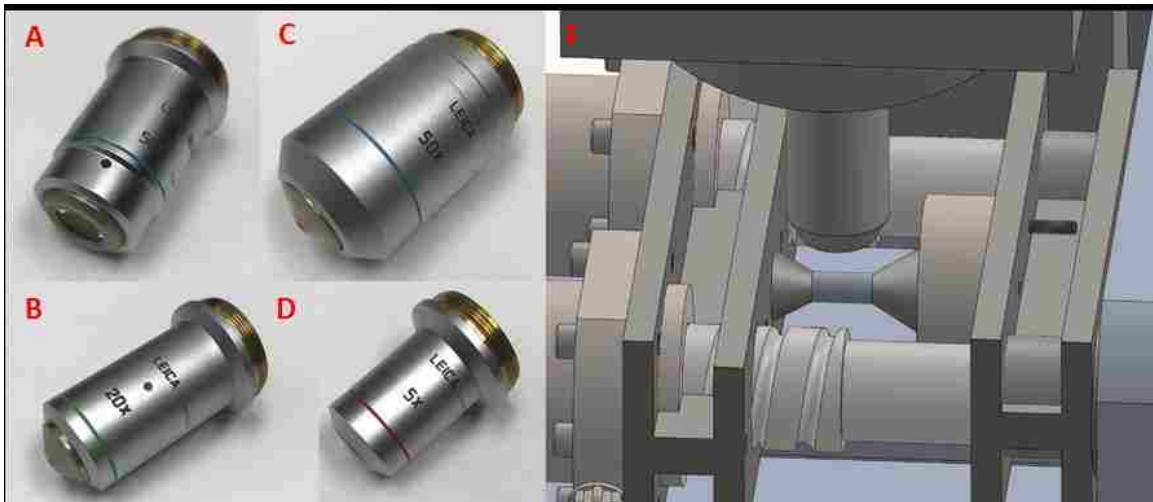
Figure 28: Microscope lenses geometries and focusing fitment.

Calculations

Analytical calculations of key system components and subsystems were performed to ensure the compression fixture could meet design requirements and to provide a better understand of system kinematics. These calculations included sample loading, ball screw load analysis, torque, gear reduction, gear spacing, and advancement rate.

<u>Sample loading</u>

The desired compressive force of the system was 14,137 N which would allow high strength ceramic specimens to be compressed to 500 MPa. Using the stress equation, the force required for samples with diameter of 2 mm and 6 mm was calculated and shown in table 1. The required force (F) was calculated using the stress equation, equation 3, using stress (σ) and cross-sectional area (A_c).

Equation 3: Required system force.

$$F = \sigma \bullet A_c \tag{3}$$

Table 1: Load due to compressing the ceramic sample to the desired stress of 500 MPa.

Sample Diameter	Cross section Area (A_c)	Total Load (F)
2 mm	3.14 mm^2	1,571 N
6 mm	28.27 mm^2	14,137 N

The maximum stress of 500 MPa can be achieved with the system designed. Each of the systems two ball screws would be subjected to ~50% of the total load. The resulting loads calculated from a uniaxial stress of 500 MPa for samples with a cross sectional area of 2 mm and 6mm (table 1).
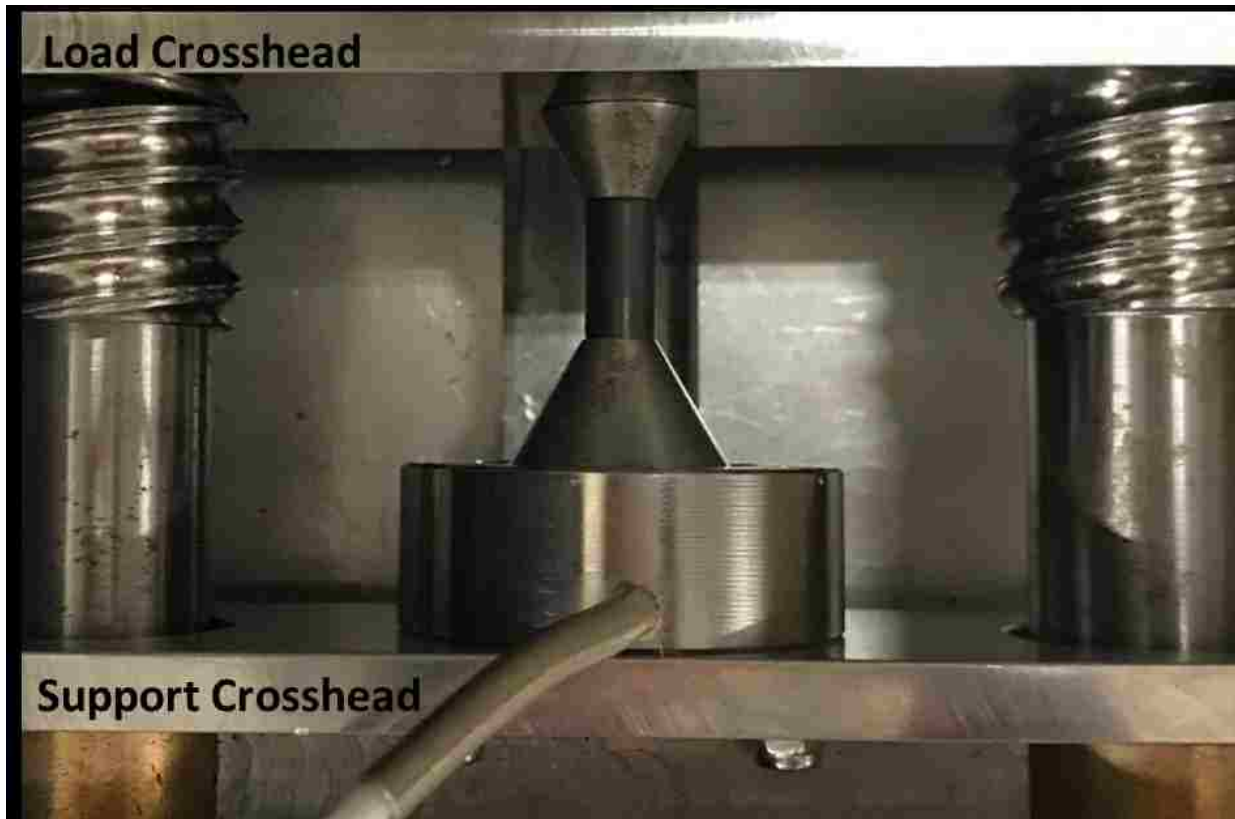
Figure 29: Sample load setup.

Ball Screws

It is important to gage if the ball screws are operating at a safe compressive force to ensure they will not buckle to deflect to a point which will compromise the compression fixtures performance. According to Thompson Linear (Thompson Linear Motion, Radford, USA), which produces ball screws, the critical buckling force (F_c) and safe compression force (F_s) are a function of root diameter (d_f), fixed end factor (C_s), and max unsupported length (L) area all important parameters for selection of the proper diameters of the ball screws as shown in equation 4 and 5 [33]. The manufacturer recommends a minimum safety factor of 0.8 when calculation the safe compression force.

Equation 4: Critical buckling force.

$$F_C = \frac{C_S \cdot 9.687 \cdot 10^4 \cdot d_f^4}{L^2} \qquad (4)$$

Equation 5: Safe compression force.

$$F_S = F_C \cdot 0.8 \qquad (5)$$

End Fixity Factor - Permissible Compression Loading		
End Supports		C_S
A	One end fixed, one end free	0.25
B	Both ends supported	1.00
C	One end fixed, one end supported	2.00
D	Both ends fixed	4.00

Figure 30: End fixity factor C_s [33].

Exceeding the recommended maximum compression force may result in buckling of the screw shaft [33]. Using a conservative approach that the ball screw is supported at both ends, the safe compressive force was calculated to be equal to 645 kN. Therefore, the ball screw is safe from buckling. It is assumed that as the travel length of the device is short, that any rotational excitations from the stepper motor will be below that of the fundamental natural frequencies within the stages

frame geometry. The critical speed of the ball screw was not taken into consideration. Vibrations were taken into consideration at all speeds and no large increases in vibration which would elude to natural frequencies occurring were witnessed.

Torque

The required torque of the stepper motor was calculated to produce a maximum clamping force of 14,137 N. The torque, equation 6, required to produce the required clamping force was calculated using a simplified equation. The torque is a function of required force (F), lead (P), gear reduction (R), and efficiency (%eff).

Equation 6: Required torque.

$$T = .177F \bullet P \tag{6}$$

The required stepper motor torque was determined to be 2.5 N-m for each lead screw. A single Stepper motor drives both ball-screws the requiring an input without a gear reduction of approximately 5 N-m. The Anaheim automation stepper motor model number 24Y304S-LW8 which is used in the system has a maximum bipolar torque output is 2.06 N-m. Therefore, a power transmission needed to be designed to reduce the required torque of the stepper motor.

Gear Reduction

To correctly size the stepper motor and gear box, the required torque of the gear box was calculated. The calculation is then used to determine the necessary gear reduction and stepper motor torque. First the terminology of lead screws and ball nuts must be understood. The lead of a lead screw or ball screw refers to the linear distance the ball nut will travel per rotation of the

ball screw. Lead screw assemblies work much like a typical screw, but use ball bearing, which rolls between the helical groves (Figure 31). The screw and nut only have contact between the ball bearing resulting in precise travel and low friction. Due to low friction, ball screws offer mechanical efficiencies and allow around 90% of the rotation motion to be translated into linear motion.
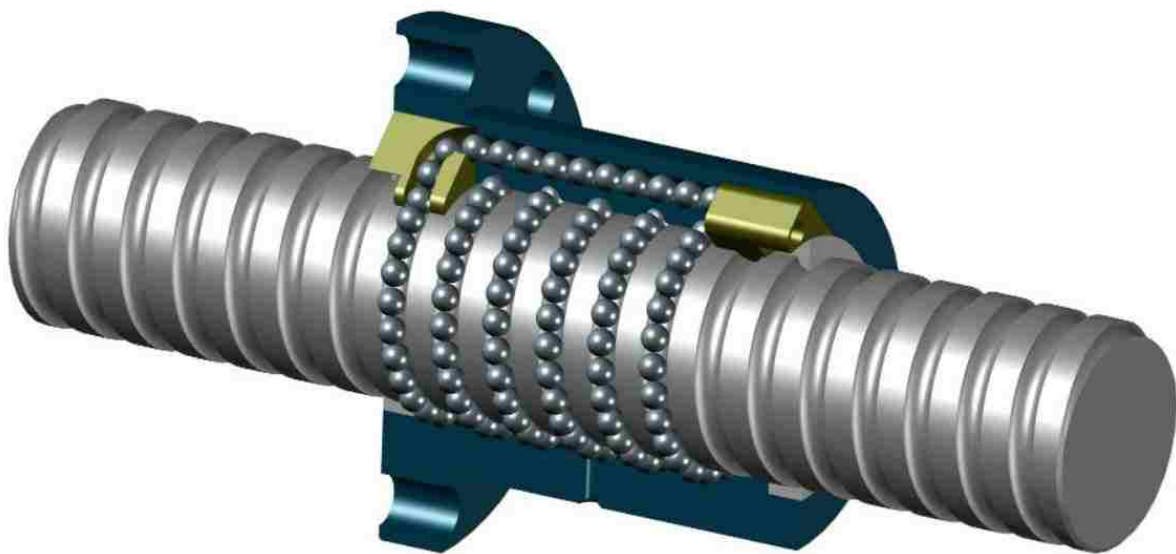
Figure 31: A schematic presentation of a ball screw with a tangential ball return system [34].

The *in-situ* compression stage used an Anaheim automation high torque stepper motor to provide rotational power to a gear train, which interns lead screws providing linear motion. A compound gear train was designed to increase the power transmission of the stepper motor to the required level. The gear ratio of the gear train was calculated using the principles in equation 7 where T_1 is the drive gear and T_2 is the driven gear.

Equation 7: Gear ratio.

$$R_{ij} = \frac{T_j}{T_i} \tag{7}$$

In the table below, the gear reduction of each stage of the gear train is shown. In order to exceed the required torque reduction a two-stage gear train was used and provided a final gear reduction of 1:16.

Table 2: Gear reduction of compression stage transmission.
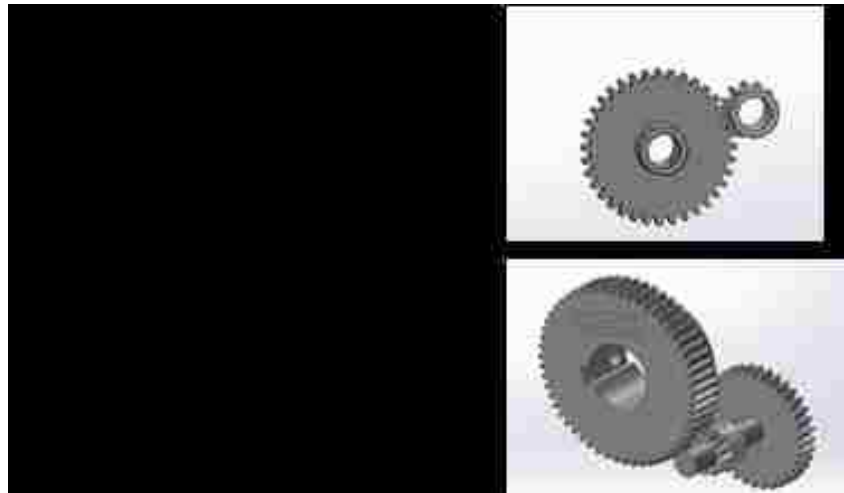
Gear Spacing

The module 1 gears used in the gear train have a 20-degree pressure angle. The required center distance needs to be calculated to determine the position of the gear shaft bearing and the stepper motor. Equation 8 was used to calculate the required center-to-center distance where pd_1 and pd_2 and the pitch diameters of gear one and two, respectively.

Equation 8: Center-to-center distance.

$$a = \frac{pd_1 + pd_2}{2} \tag{8}$$

The center to center distances was calculated to allow to proper gear clearance in the design. The schematic drawing used to understand center-to-center gear spacing, clearance, and gear terminology is shown in figure 32.
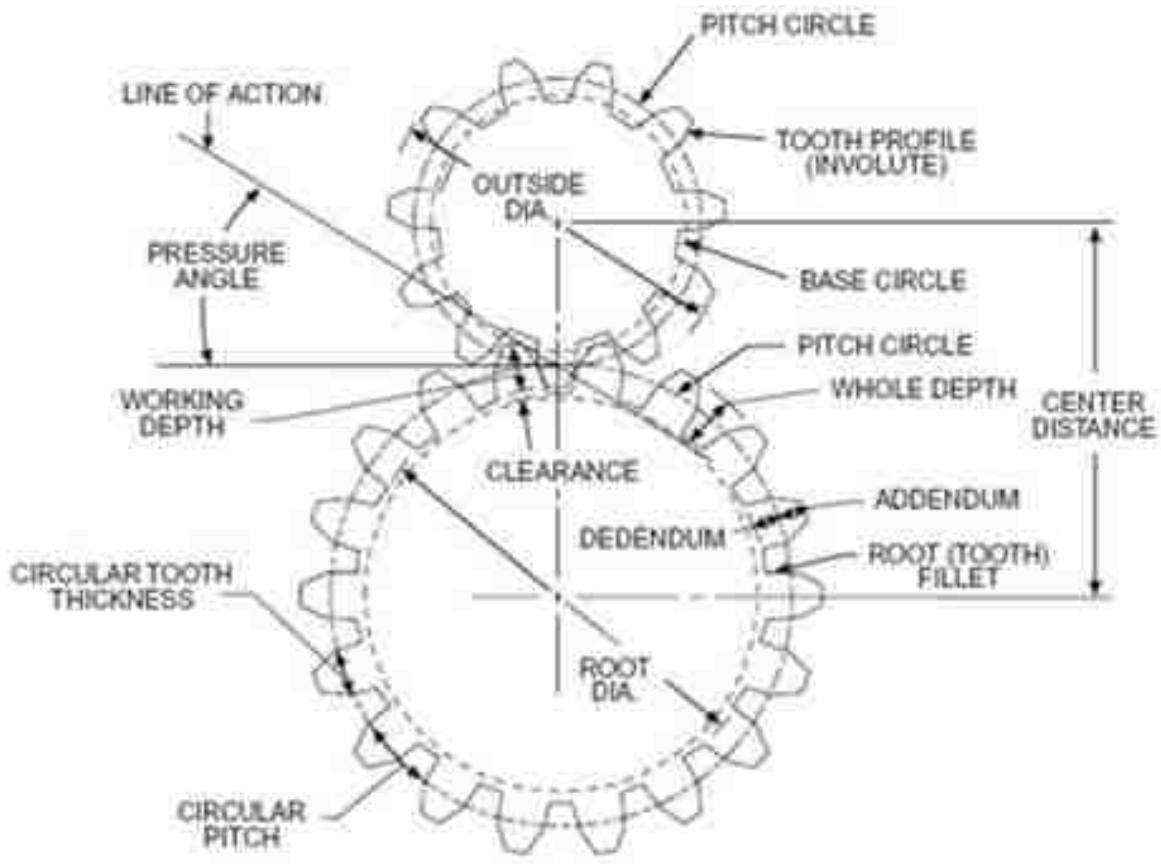
Figure 32: Drawing of Center to Center Distance of spur gears [35].

44

The required center distance between gears one and two is 24 mm. Likewise, the required center to center distance between gears three and four is 33.5mm. The calculations were performed using the manufacturer's specified pitch diameter.

Load Rate

Understanding the advancement rate of the load crosshead versus the rotation of stepper motor is important to determine the correct rotation rate of stepper motor to achieve a desired load rate during testing. The ball screws used, have a lead (p) of 10mm. Therefore, for every rotation of the ball screw, the ball nut and crosshead attached advance 10mm. Due to the 16:1 gear reduction (R), the ball screws advance 0.625mm per rotation of the stepper motor. This advancement rate can be controlled by adjusting the frequency of the step clock input (f) which will be explained in greater detail in the system control section. For most loading conditions, a micro-step resolution of 50,000 steps per revolution will be selected. Therefore, for every 50,000 step clock inputs, the motor will complete one revolution. The crosshead speed or load rate ($\dot{k}$), mm per minute, for different step clock inputs can be calculated using equation 9.

Equation 9: Crosshead speed.

$$\dot{k} = 0.00075 \bullet f \tag{9}$$

Using the crosshead speed, the strain rate of an experiment can be calculated by dividing the crosshead speed by the gauge length of the specimen. This information could be critical if it is desired to test samples at a specified load or strain rate.

45

CAD Design

An initial complete redesign of the compression stage was performed in SolidWorks. An in-depth design process was started by studying "Lesson learned" from past designs. This included misalignment issues, deflection of the components and their selection. This knowledge was leveraged when designing components such as the aluminum stage, crossheads, transmission, and ball screws in SolidWorks. Commercially available components were also modeled whenever the CAD files were unavailable. This allowed the complete compression stage to be designed and modeled insuring component fitment during assembly.

One challenging aspect of the design was incorporating components which had already been purchased by the second senior design team even though their design was not finalized. Items which were already purchased included the ball screw material stock, ball nuts, the stepper motor, transmission gears, and transmission shaft material. To add to this challenge, several of the components available were improperly labelled in the material order documentation, were the incorrect size, or not used in the CAD model. For example, the gears purchased for the compression stage had a journal diameter of 25 mm and the recommended ball screw machined diameter was 20 mm. This lack of design documentation and insight made improving the original design almost as hard as starting from a fresh slate.

A design review was performed including other engineering students and machinists at the UCF machine shop. This collaboration with experienced machinists helped streamline the design and manufacturing process. Also, reduced machine time and cost were additional benefits of directly working with the machinist at the UCF CECS machine shop.

The following major changes were performed.

1. Constraining the lead screws using ¾-10 and ½-13 fasteners.

2. Adding fasteners to required locations.

3. Developing a way to constrain the stepper motor.

4. Eliminating the curves on the stage plates to allow a standard key cutter to be using during machining.

5. Including platen which would compress the sample.

6. Changing thickness of the stage plates to match bearing thicknesses.

7. Eliminating the complex curves on the sample support stage.

8. Adding bushings for the transmission shafts and load crosshead to reduce wear and friction.

9. Reconfiguring the gear system to reduce the footprint.

10. Changing the geometry of the load crosshead to allow for the ballnuts to be mounted.

11. Commercially available parts without models were re-drawn to improve model quality.

The differences between the initial senior design and the final design which was produced are clearly displayed in figure 33. As listed above, fasteners were added to constrain the components and parts of the compression stage. The stepper motor was moved to allow it to be bolted to the aluminum plate instead of floating unconstrained. The motor plate and midplate were also redesigned including an upper area for the transmission shafts and associated bushing to be mounted. Ball screw journal diameters were adjusted to the appropriate manufacture recommended journal diameter and spherical ball bearing were used. The stage was simplified to allow ease of manufacturing and reduce machining time. Also, components such as the load cell and platens were added to allow the microscope lenses to reach the required working distance.

Although the original senior design team had multiple mistakes in their design, documentation, and component selection, as mentioned in the literature review, the senior design team did have many great engineering ideas. This included making the compression stage fixture out of multiple parts, using I-beams for the load and support crosshead, and the concept of the two-stage transmission.
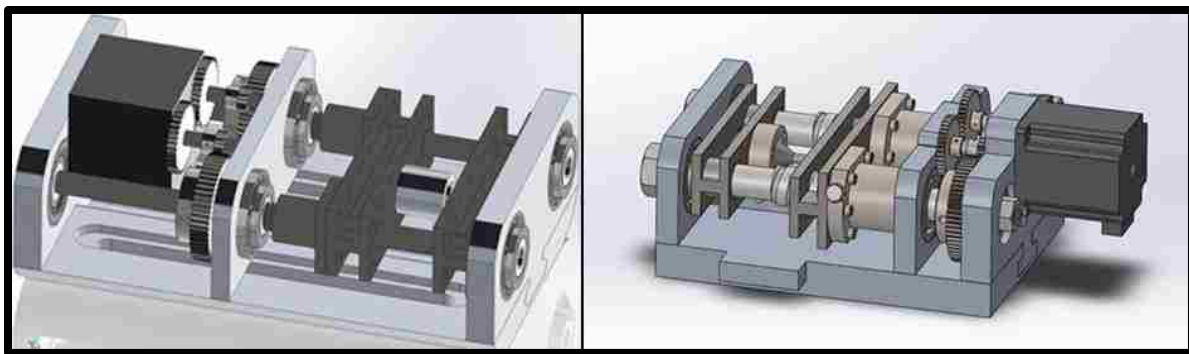
Figure 33: Initial compression stage design (left) and final compression stage design (right).

In the following paragraphs the mechanical aspect of the electromechanical compression stage design. The terminology for subsystems is outlined in figure 34 which include; the ball screws, the support crosshead, the ceramic sample, the load crosshead, the ball screws, the gear train, and the stepper motor. The design of each of these subassembly and individual components are reviewed in the following sections.
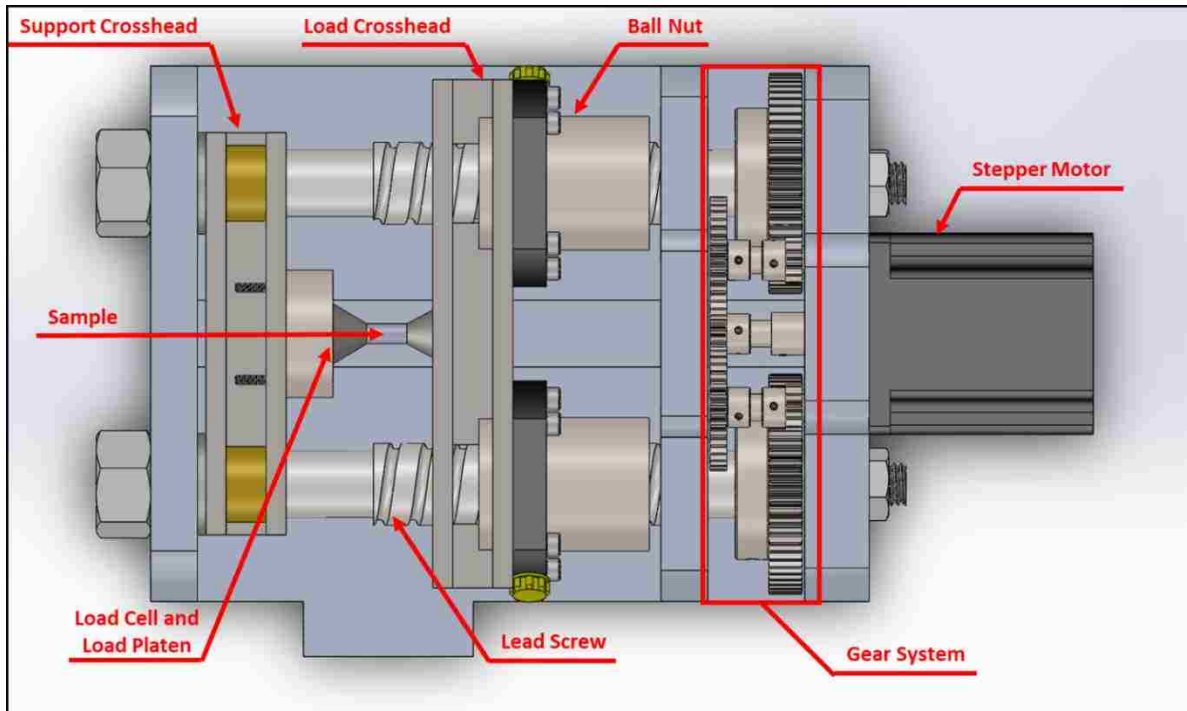
Figure 34: Components of the compression stage fixture.

The compression fixture was designed to minimize loading into the aluminum support fixture or backbone and instead constrain the primary load path to the ball nuts, support crosshead, and load crosshead. A simplified free body diagram can explain this concept. Torque is input into the ball screws via the large main gears spinning the lead screws. The ball screw and ball nuts apply force into the load crosshead advancing it by 10 mm per revolution compressing the sample. An equal force is exerted on the load crosshead and support crosshead because of the platens, ceramic sample, and load cell. The force of the support crosshead travels through the inner ball bearing races (not shown) which are constrained by ¾-10 fasteners and thus are transmitted back to the ball screws themselves.
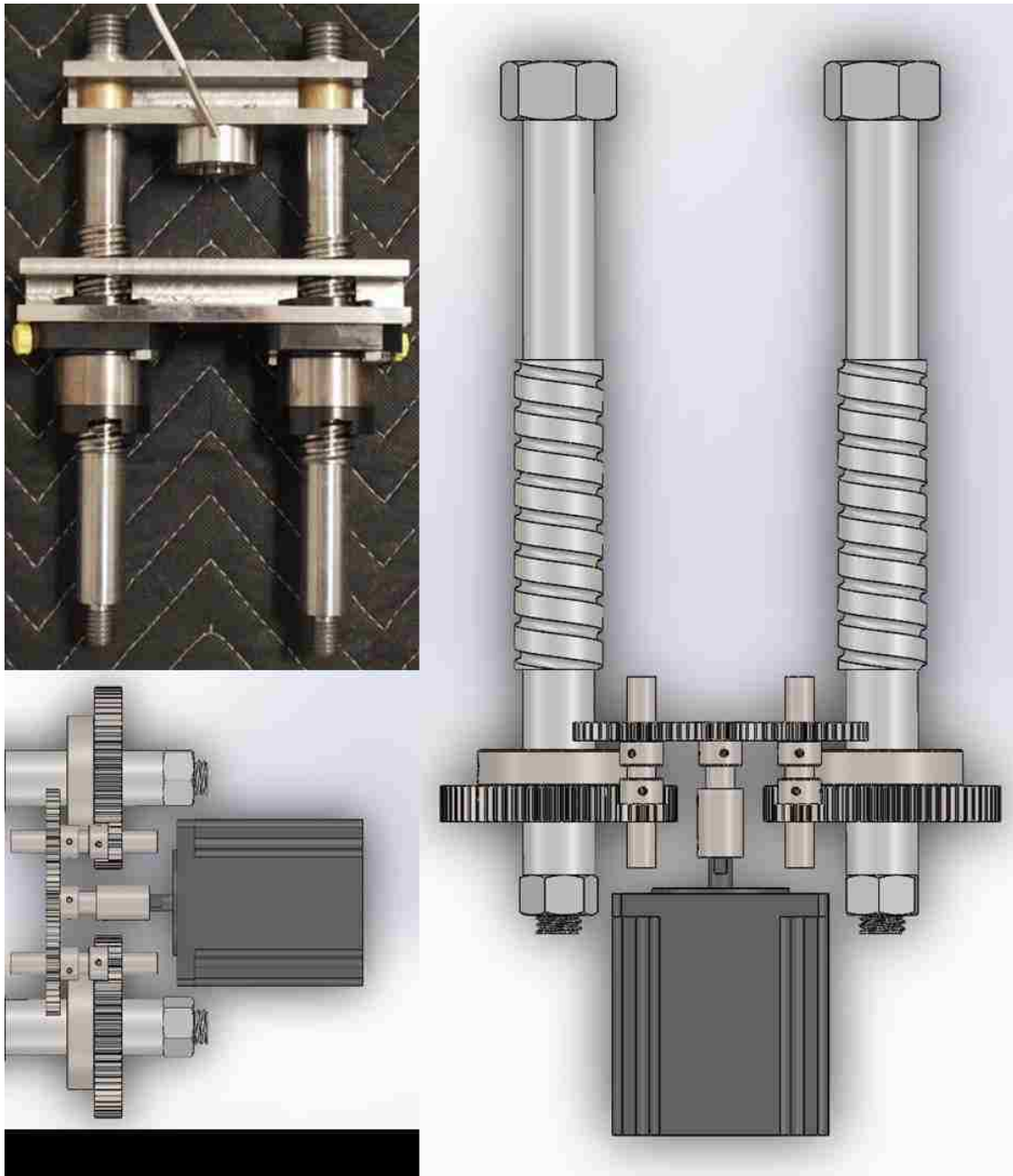
Figure 35: Compression fixture load system: Ball screws, load crosshead, support crosshead, gears, and stepper motor.

Thompson 25mm Ball Screw and 25mm Ball Nut part numbers 7832786-P5 and 7832787 are used to drive the load crosshead and compress the sample. The ball screw bearing journal diameter was

machined to 20 mm as recommended by the manufacturer. The 20 mm journal diameter was machined so that the ball nut would fit into all three bearing supports yet allowed the ball nut to advance all the way without hitting the end of the threads therefore eliminating the opportunity for the ball nut to run off the threaded portion. To ensure that the ball screw each side is secured a bolt which are a ¾-10 thread and ½-13 thread were used. The motor size fastener used in the design was ½-13 because of stepper motor clearance and because it is not in the load path of the compression crossheads.
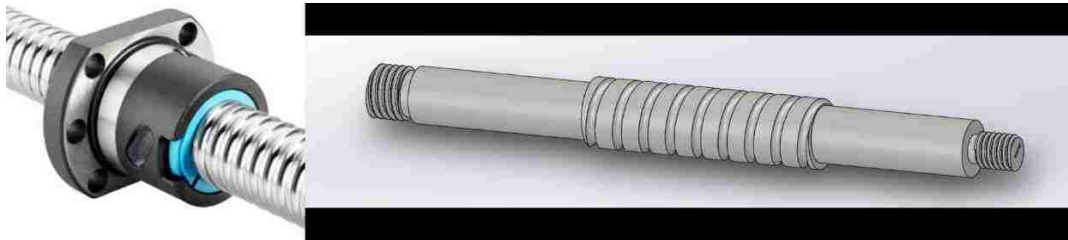
Figure 36: A photo of Thompson linear ball screw and ball nut, along with SolidWorks model of a ball screw [33].

The support-crosshead assembly includes a custom I-beam machined at the University of Central Florida Machine shop of 440C grade stainless steel (figure 37). Support crosshead is aligned on the ball screws using two bronze sleeve gears McMaster-Carr part number 6658k44. Also, an Omega LCGB-10K load cell is used to measure the compressive force of the system.
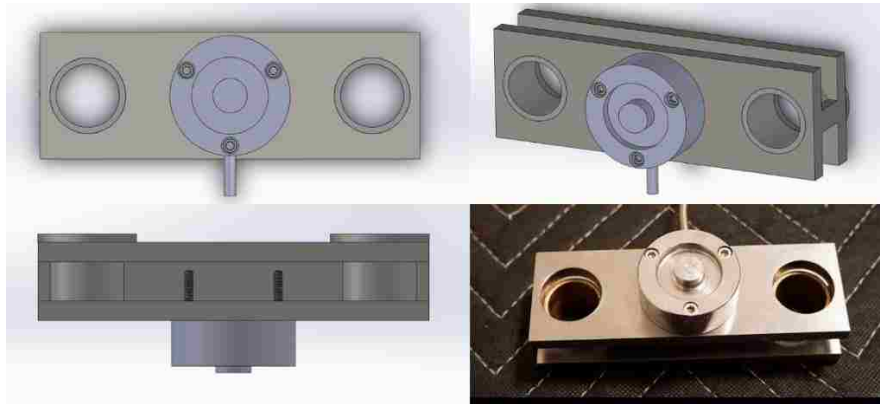
Figure 37: Support crosshead subassembly.

Likewise, the load-crosshead assembly uses 440C stainless steel and was designed as an I-beam to increase the moment of inertia while decreasing weight. A load platen made of 4140 steel is press fit into the member. The load-crosshead is shown with the Thompson ball nuts attached, which are fastened using M5 socket head screws (figure 38).
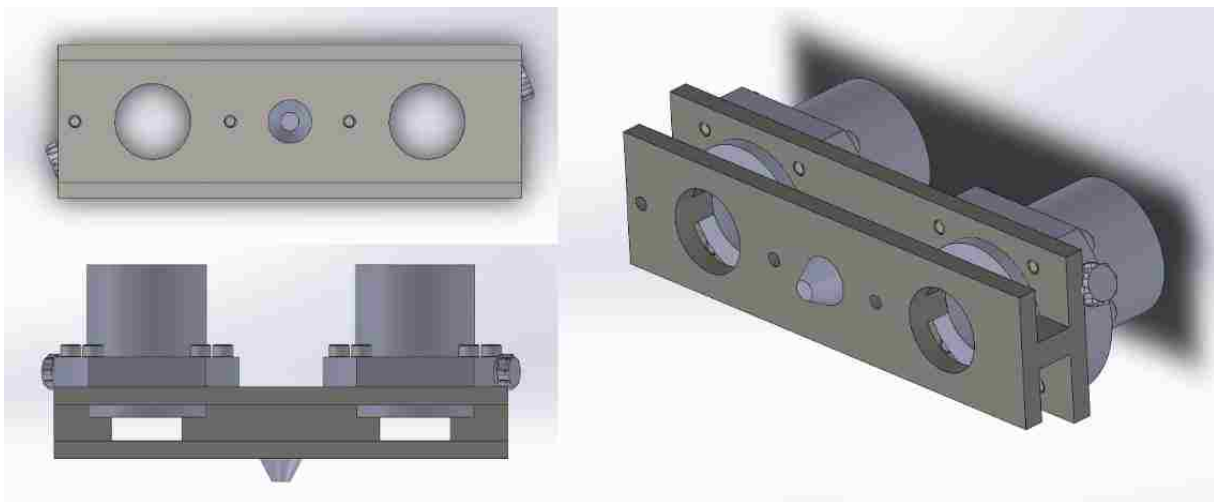
Figure 38: Load crosshead subassembly.

The fixture backbone is constructed of four individual pieces of 6061 aluminum shown in figure 39. McMaster-Carr, 20mm journal diameter heavy duty ball bearings are used to constrain the ball

screws. McMaster-Carr part number 6679K12 8 mm sleeve bearings were used for the transmission shafts. The four-piece construction was utilized because it allows easy assembly, can be machined from less expensive aluminum plate stock. This design also allows to reconfigure of the compression stage for different sample sizes and possibly tensile testing in the future.
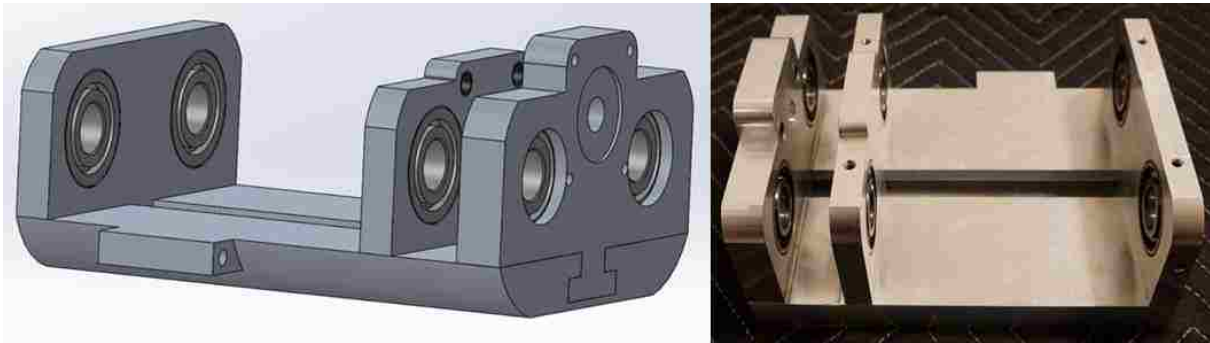
Figure 39: Compression stage CAD model and machined Assembly.

The gear reduction transmission which utilizes 7 gears to produce a final gear reduction of 16:1. Module 1 gears were used and included; three 12 APW Wyatt part number 85032 gears, two 36 tooth part number unknown gears, and two 64 tooth KHK module1 part number SUS1-64J20. The input and intermediate shafts were cut and machined from 8 mm shaft stock. A setscrew shaft coupler (not shown) Servo City part number 625185 is used to adapt the ¼" diameter stepper motor drive shift to the 8mm input shaft.
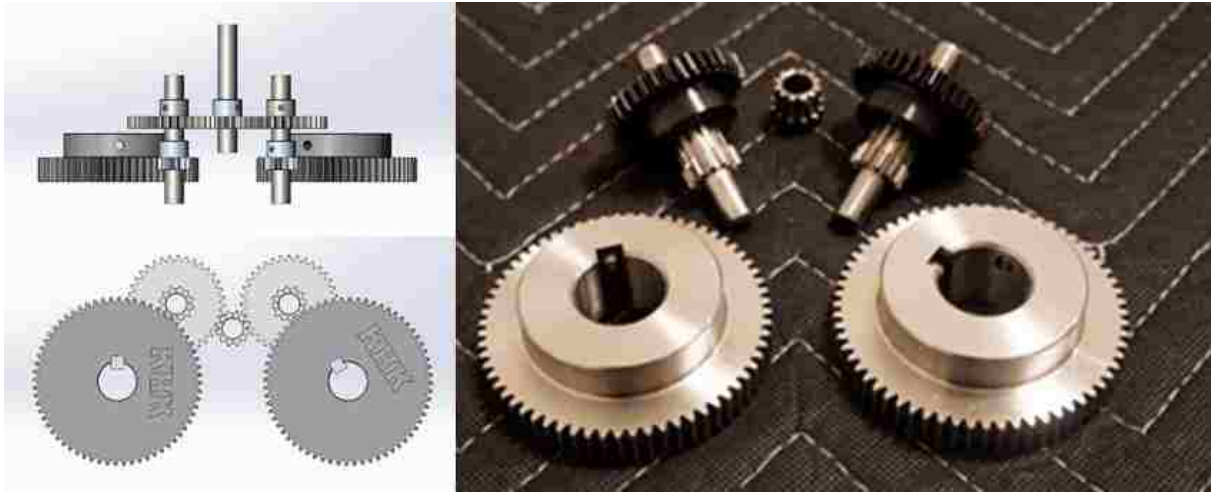
Figure 40: Transmission gears design and machined components.

Microscope stage mounting fixture was machined from 6061 aluminum and is mounted to the Leica optical microscope using four M4 socket head screws. Using the microscopes focusing fixture as a z-axis reference, the mounting fixture was designed to allow the stage to be shifted in the x and y axes directions, which allowed for some adjustability of the focal point of the ceramic sample during focusing event.

Figure 41: Compression stage mounting fixture.

Finite Element Analysis

A finite element analysis using Siemens NX 11.0 was performed on the load crosshead and support crosshead to calculate the stresses and magnitude of deflection which is expected to occur. The cross-sectional area of the crossheads utilizes an I-beam shape to minimize weight and increase the moment of inertia, reducing the deflection. The load-crosshead and support-crosshead was machined from 440C stainless steel. ASTM A276 standard grade 440c stainless steel is a high carbon martensitic stainless steel, providing good corrosion resistance, extreme high strength, and hardness [36].

Load Crosshead

The compression stage load crosshead FEA model was developed using the following parameters. A 3D tetrahedral mesh with an element size of 2.54 mm was used for the ball nuts and I-beam. Also, a 3D tetrahedral mech with an element size of 1 mm for the load platen. For the boundary conditions, a fixed constraint was applied to the inner diameter of the ball screws. Also, surface-to-surface contact constraints were implemented between the I-beam and the ball screws. A force of 14137 N was applied to the load platen.
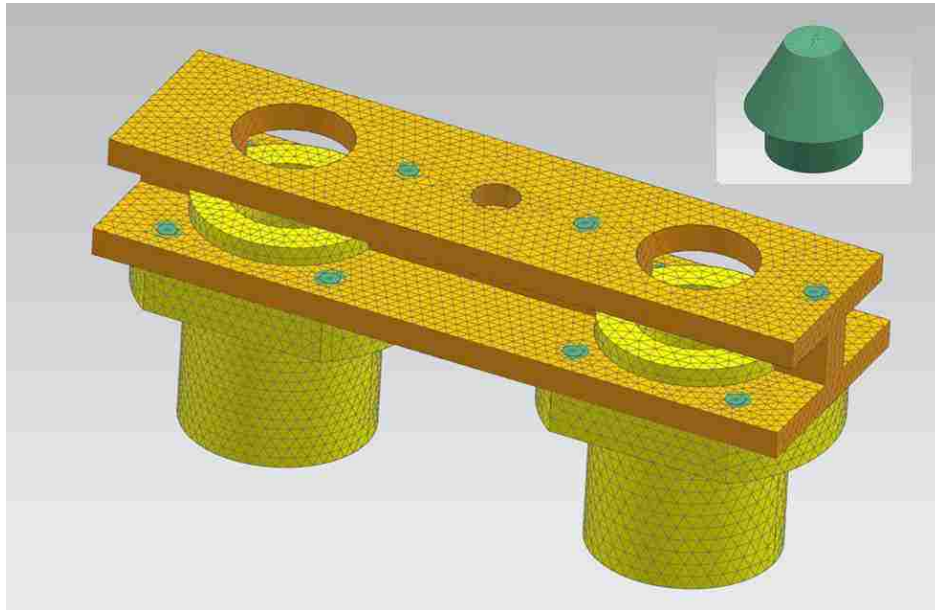
Figure 42: Finite element model of Load-crosshead and load platen.
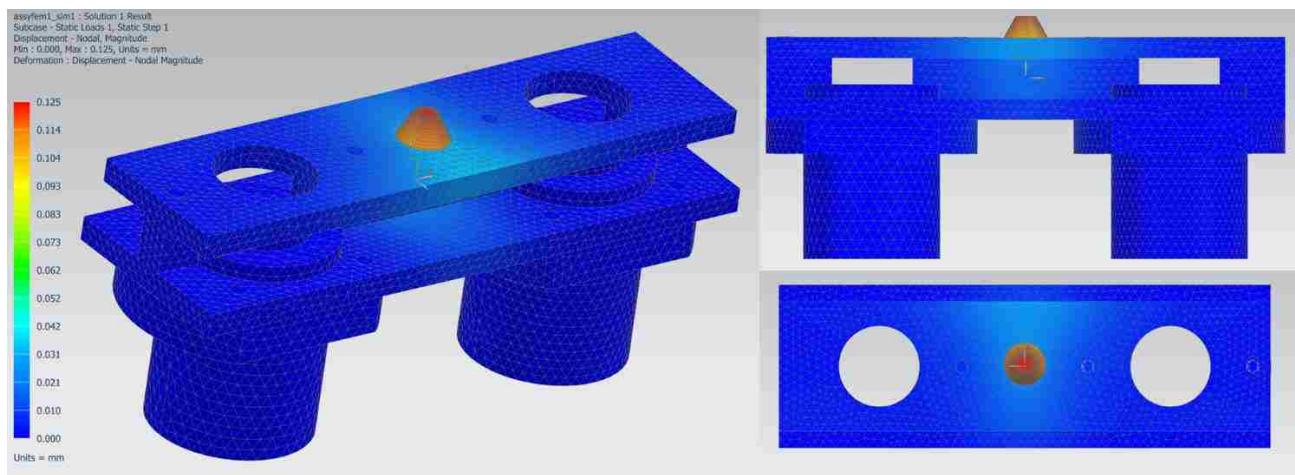
Figure 43: Compression stage load I-beam FEA deflection results.
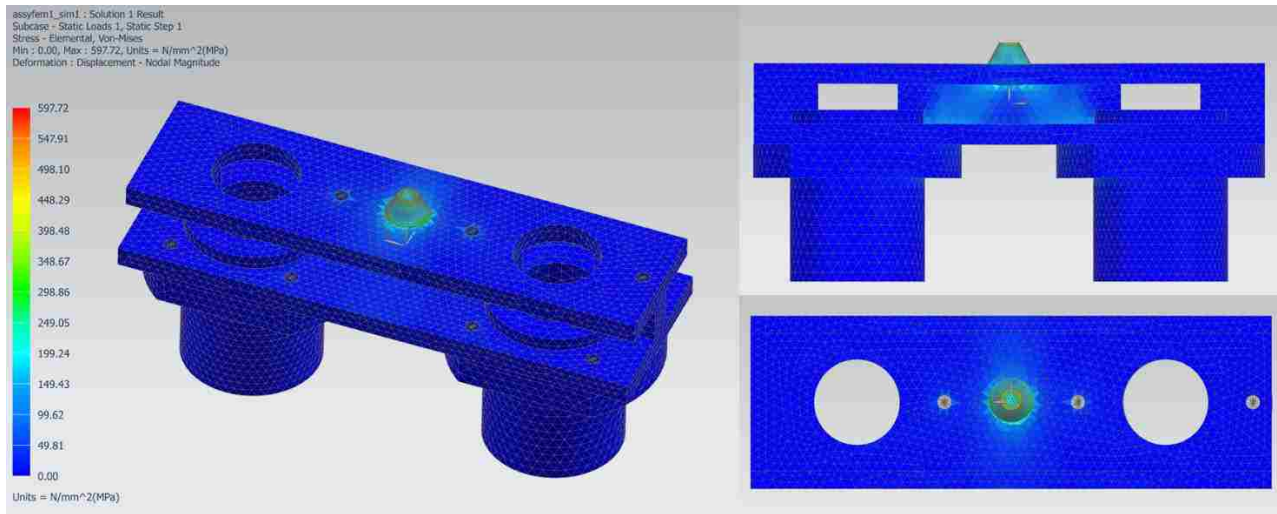
Figure 44: Compression stage load I-beam FEA stress results.

The load cross head also has surface-to-surface contact results because it was modelled as an assembly with the load screw ball nuts.
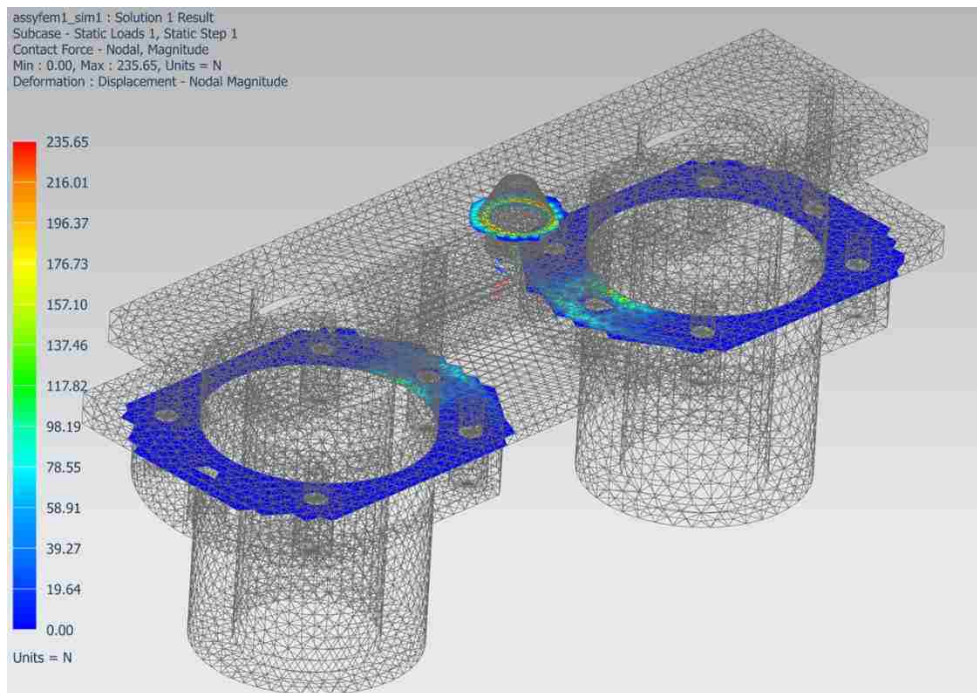
Figure 45: Compression stage load I-beam FEA surface-to-surface contact stress.

Support Crosshead

The compression stage support crosshead FEA model was developed using the following parameters. A 3D tetrahedral mesh with an element size of 2.54 mm. The boundary conditions were applied to the bottom rings where the I-beam would contact the compression stage frame. A force of 14137 N was applied to the circular area where a load cell is mounted to the I-beam.
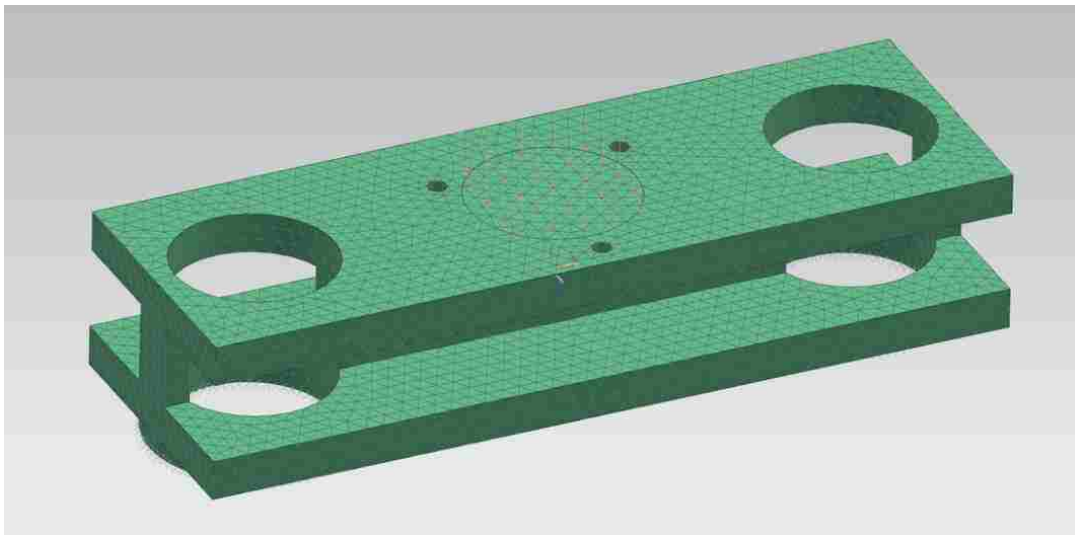
Figure 46: Finite element model of compression stage support crosshead.
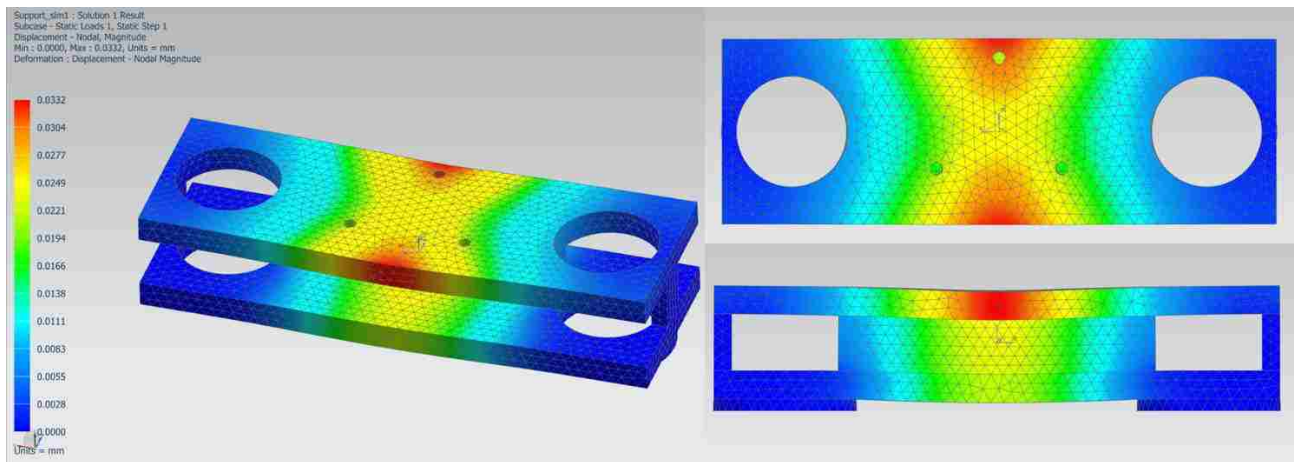
Figure 47: Compression stage support I-beam FEA deflection results.
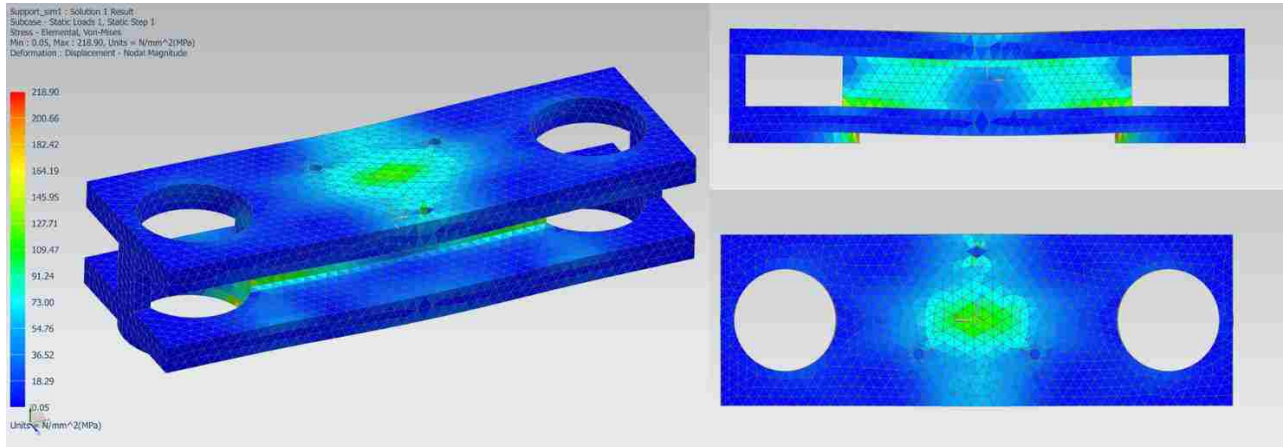
Figure 48: Compression stage support I-beam FEA stress.

Results

The maximum stress of the load and support I-beams were 278 MPa and 186 MPa respectively.

The material of the load and support I-beams, 440C stainless steel, has a minimum yield strength

of 450 MPa and a minimum ultimate strength of 760 MPa [37]. Using this information, the margins

of safety for the load I-Beam and support I-Beam were calculated using equations 10 and 11 and

are presented in table 3.

Equation 10: Margin of safety yield.

$$MS_{yield} = \frac{\sigma_{yield}}{\sigma_{max}} - 1 \tag{10}$$

Equation 11: Margin of safety ultimate.

$$MS_{ultimate} = \frac{\sigma_{ultimate}}{\sigma_{max}} - 1 \tag{11}$$

59

Table 3: Load and support I-beams margins of safety.

Component	σ_{max}	MS_{yield}	$MS_{ultimate}$
Load I-Beam	278 MPa	0.62	1.73
Support I-Beam	186 MPa	1.42	3.09

Although Margins of safety to yielding were relatively low, these stresses were concentrated in small regions near load platens and supports. Also, deflections were minimal and should not significantly affect experimental results. After completing the finite element analysis, it was determined the stress and deflection of the 440C stainless streel load-crosshead and support-crosshead was acceptable.
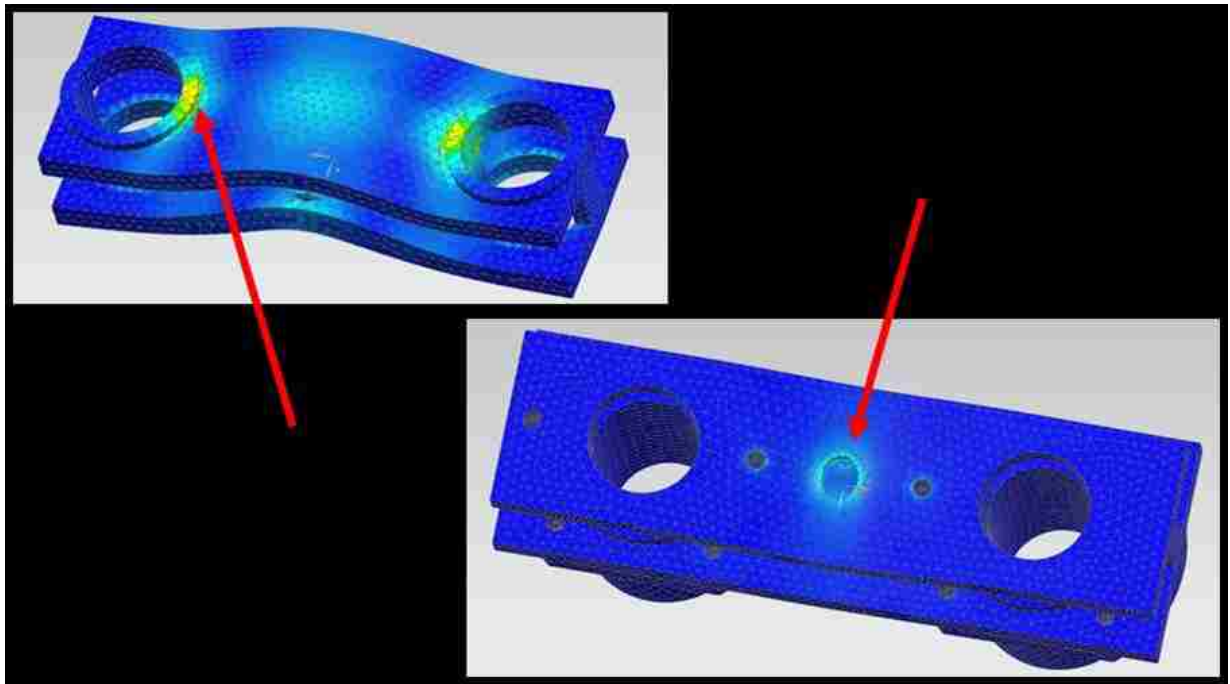
Figure 49: Finite element analysis max stress locations.

Manufacturing and Assembly

After the compression stage was designed, the next step was to manufacture components which were not commercially available. Machining of these components was performed at the UCF College of Engineering and Computer Science (CECS) machine shop using a mixture of manual controlled machines and computer numerical control machines. Drawings produced using SolidWorks were used by the UCF machine shop machinists to machine the parts. For parts which were machined using CNC machines, the CAD files were also provided. Critical features were machined to a tolerance of 0.127 mm (±0.005).

Figure 50: UCF machine shop vertical mill (left) and load cell alignment (right).

The components were assembled after bring machined. Some of these assemblies needed high accuracy alignment and were assembled using a three-axis end mill, edge finders, indicator, and gage pins. For example, the load cell platen needed to be centered between the ball screws in order to centrically load the ceramic sample. This was achieved by indicating the centers of the support crosshead bushings and then using a gage pin to roughly center the load cell and load platen. Next, an indicator was used to center the load cell to approximately 0.0254 mm (±0.001) shown in figure 51. The gage pin was again used to apply a load to steady load cell and platen while the M4 bolts were secured. Last, the platen was indicated to ensure the load cell did not move while being secured.
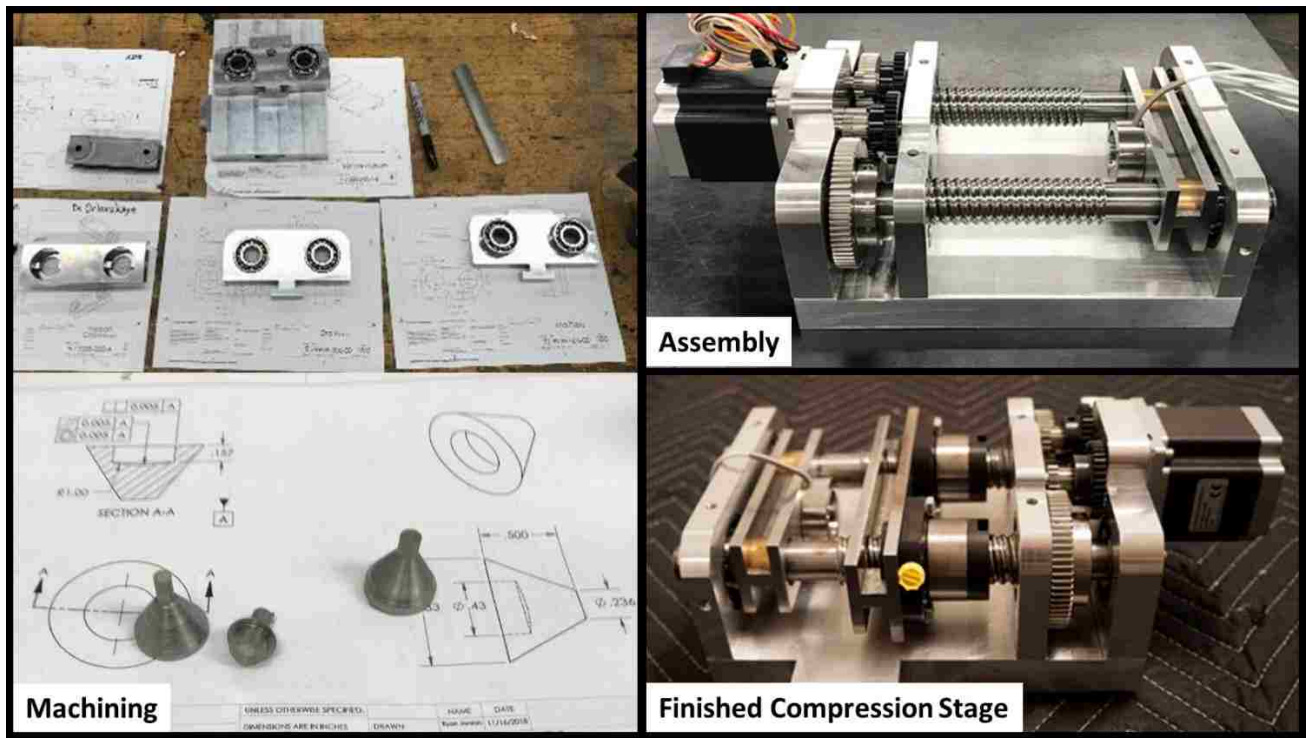
Figure 51: Compression fixture machining, assembly, and finished compression fixture.

General assembly was achieved by lubricating the parts with a light film of oil before sliding them into place. Press fit components were pressed into position using a manual press. For components where the press fit alignment was critical, like the load and support platens, components were first aligned using the three-axis mill and a gage pin to ensure they were straight and perpendicular. Then the pressing procedure was initiated using the mill before finishing the pressing using the manual press. The ball nuts were assembled onto the ball screws using the procedural video on Thompson website [33]. The finished assembly of the compression stage is shown in figure 52. Overall, all the components had good dimensional tolerancing and were able to be assembled easily. Some components needed to be lightly machined and sanded in order to achieve the desired slip fitment.
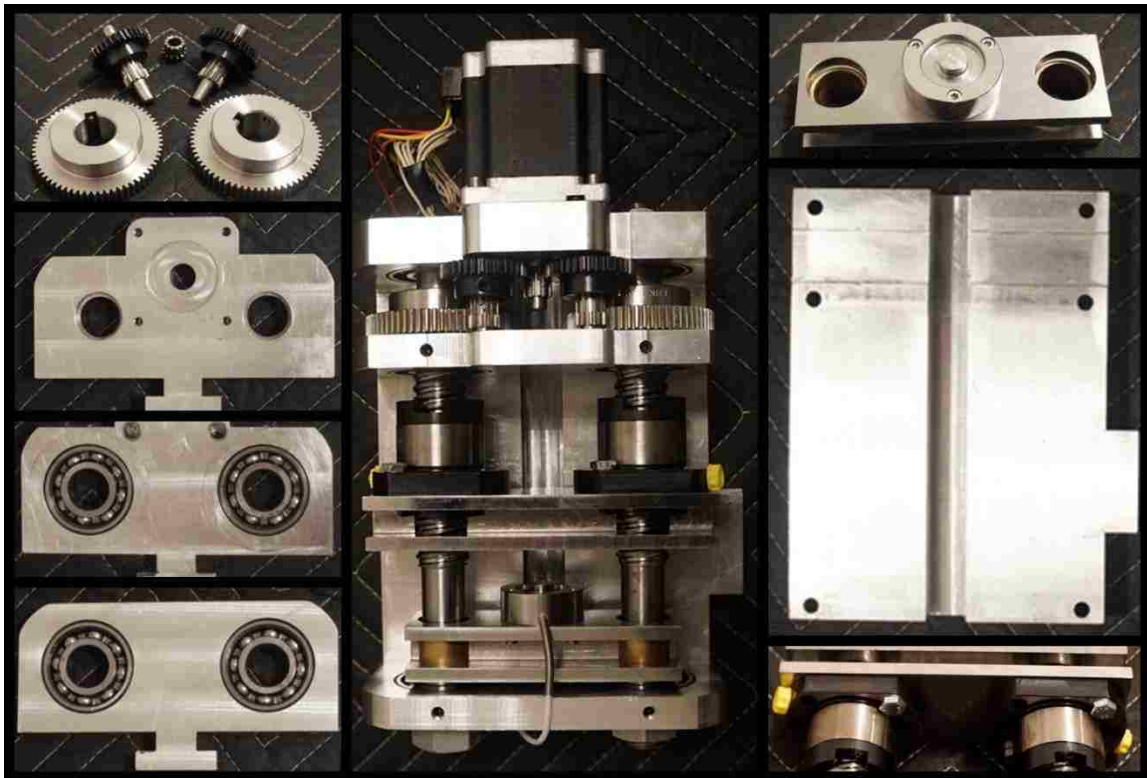
Figure 52: Final Compression stage assembly and components.

CHAPTER 4: CONTROL SYSTEM
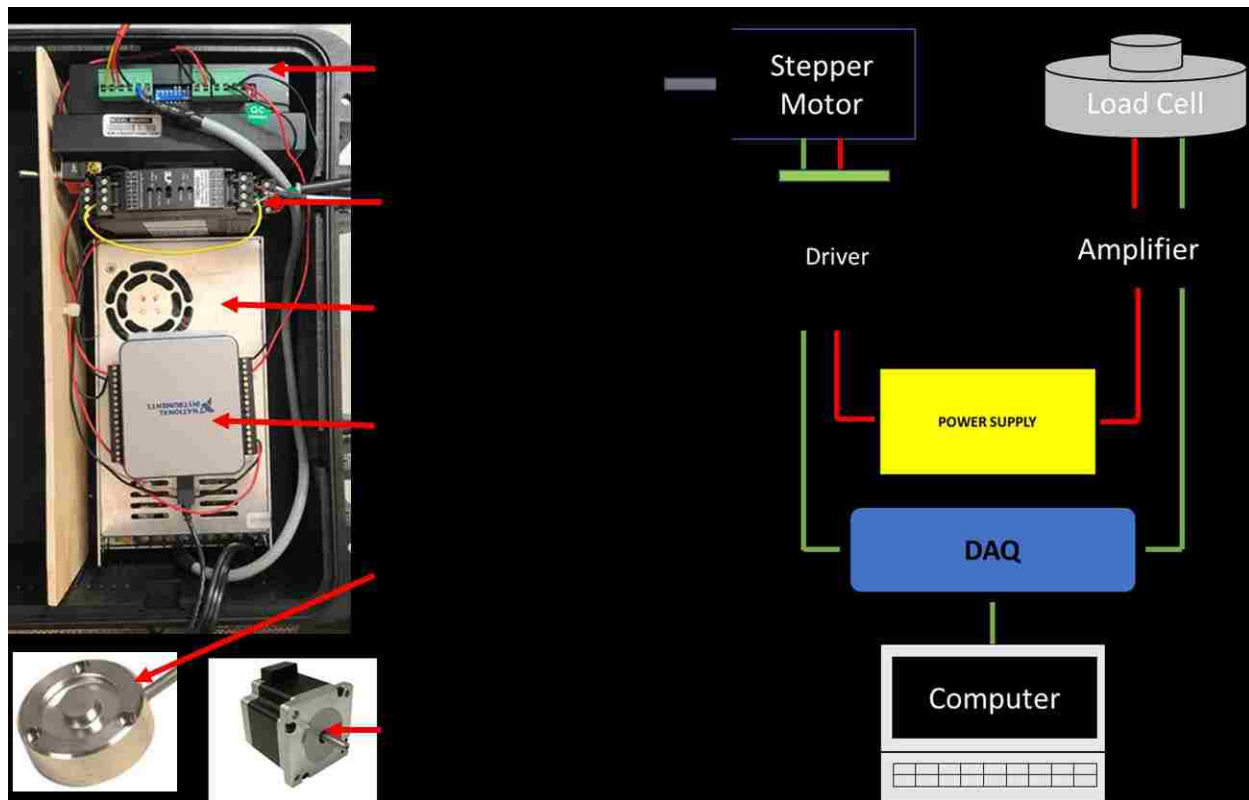
Figure 53: Control system components.

LabVIEW and a National Instruments USB-6002 Data Acquisition device is used to send a step clock input to the stepper motor driver and receive voltage differentials from the omega stain gage and signal conditioner. A DC Power Supply model number S-350-48 is used to power the stepper motor driver. The MA860H high performance micro-stepping driver is used in conjunction with the Anaheim Automation model 24Y304S-LW8 high torque stepper motor to provide the required torque to the compression stage. The 24Y304S-LW8 is a single shaft motor capable of producing

64

2.06 N-m while only weighing 0.51 Kg. Force data is recorded using an Omega DMD4059 strain gage signal conditioner and an Omega LCGB-10K miniature compression load cell.

Stepper Motor Control

The stepper motor driver and the stepper motor are turned on and off by applying 5V to the ENA input of the stepper motor driver. This connection is attached to the DAQs 5V power output and ground. Therefore, the stepper motor is engaged when it is plugged into the computer. The analog output function of the DAQ is used to send a pulse width modulation (PWM) signal to provide the required step clock input to stepper motor driver. Likewise, the direction of the stepper motor is controlled using a simple switch. When the switch is on the motor revolves in one direction and it reverses when the switch is turned off. The driver uses an 8-bit DIP switch to set micro step resolution and for most loading applications this will be set to 50,000 steps per revolution. Therefore, the PWM pulse signal must signal 50,000 times for 1 revolution of the motor. The frequencies of the PWM signal is controlled in LabView, which will communicate into the user interface section.

Load Cell Sensor measurements

The Omega LCGB-10K miniature industrial compression load cell was used because of its small thickness and ability to provide long-term stable measurements in harsh conditions and is used to convert the force applied into an electrical signal. An Omega DMD 4059 strain gage to DC isolated transmitter is used to excite the load cell and amplify the signal. Important load cell specifications include an excitation voltage of 10 Vdc which applied using the Omega DMD4059 which has an adjustable excitation power supply. The output or expected difference voltage at full load of the

load cell is 2 mV/V, and thus, the expected full load voltage would be 20mV, therefore, the Omega DMD4059 amplifiers boost the signal level to a level which the DAQ can measure. This also increases measurement resolution and improves signal-to-noise ratios. In the case of the load cell sensor measurement subsystem the DAQ is used to digitize the incoming analog signal so that computer software's in this case LabView can interpret the data.

User Interface

The system design platform LabVIEW 2017 from National Instruments was used to control the stepper motor and perform data acquisition for the load cell. A block diagram of the system was created in the visual programming language. The finished product is then operated using the interface called the front panel. Two separate front panels were developed for the load cell and stepper motor. This is so the load cell could be continuously monitored even when the stepper motor is not in use. This is especially important in early testing because it allowed the load to be monitored while spectral acquisitions were being collected using the Raman spectrometer. The load rate of the compression stage was controlled by changing the frequency of the PWM pulse signal. The calculated load and stress could also be monitored during load application simultaneously. In the future, a program which allows the system to load the sample to a specified load without human interaction will be developed.
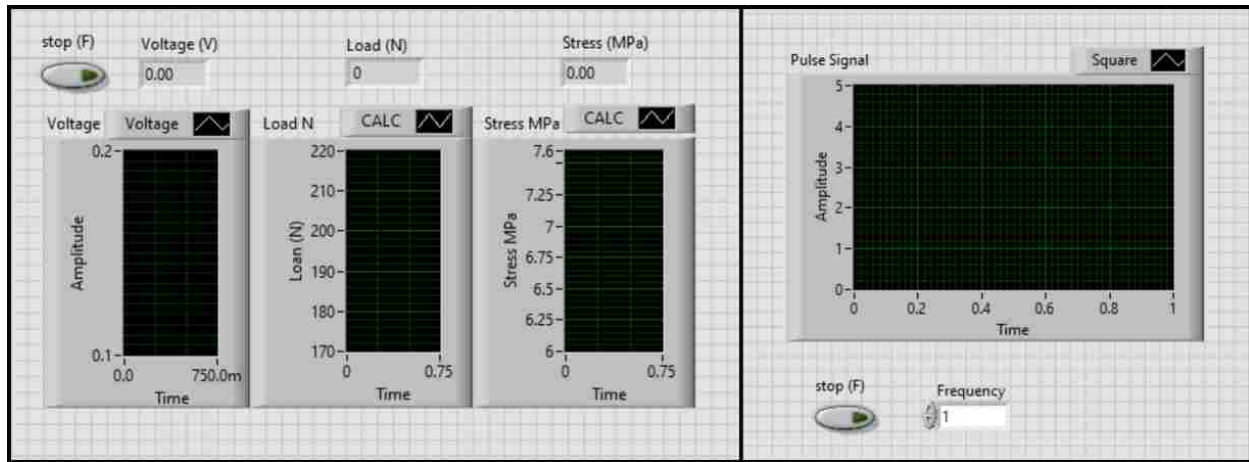
Figure 54: LabVIEW front panel.

CHAPTER 5: TESTING AND INTEGRATION

The compression stage and its systems were rigorously tested to ensure system seamless functionality and eliminate any possible problems for the operation. Majority of the problems uncovered during testing of the stage were fixed and a few remaining ones will be corrected in the future.

Compression Fixture Bench Testing

A preliminary test bench was fabricated to test the functional ability of all major systems and components. Bench testing also allowed for individual subsystems to be validated as well as trouble shoot problem. Major accomplished milestones included: the microscope fit check, cycling the system, and application of the compressive load to a test ceramic sample. Also, at this time, proof testing was performed to ensure the compression stage drive system and structural components could handle the required stress of the system.
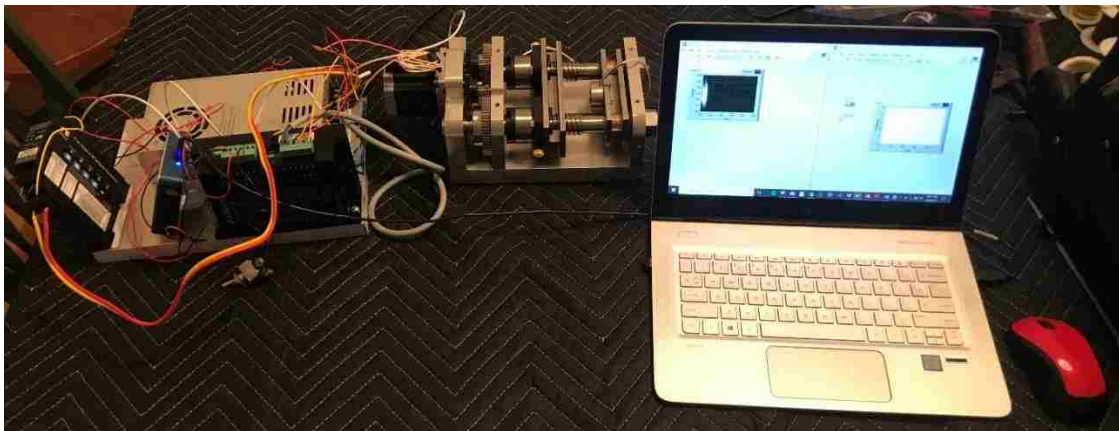
Figure 55: Bench testing of the compression stage.

Load Cell Calibration

The load cell was calibrated using of the MTS Criterion 43 universal testing machine. The proper system calibration included aligning the whole support crosshead at the center of the MTS platens, compressing the load cell to different loads and recording the resulting voltage using the USB-6002 DAQ.

Figure 56: Load Cell Calibration using MTS Criterion Model 43 universal testing machine.

First, because pre-strained installation condition can generate nonzero initial voltage offsets. The initial voltage offsets were compensated effectively by bridge balancing the Omega DMD 4059 amplifiers by using the built-in offset. After the voltage offset was zeroed, multiple measurements

69

at increasing loads were recorded. The electrical measurements were scaled to engineering units by recording electrical values and physical force measurements acquired from MTS universal testing machines software. A specified load was applied for each data point using MTS universal testing machine. Excel was using to determine a linear coefficient to be used for scaling.
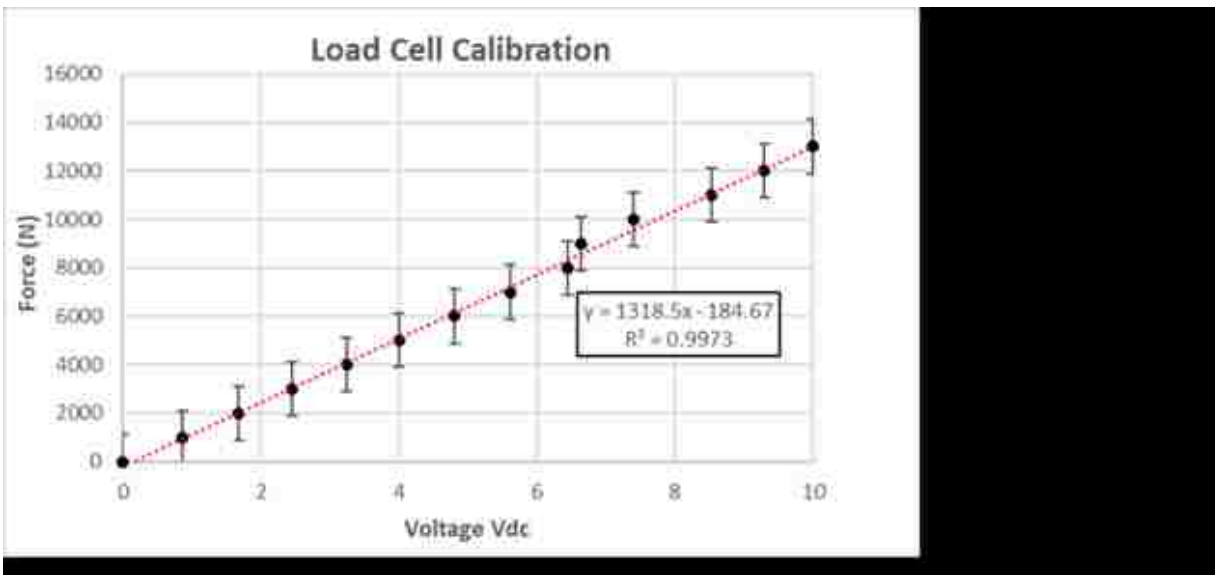
Figure 57: Load cell calibration graph.

The voltage vs. force linear equation which was determined after the calibration procedure was then used to update the LabView program so force and stress values could be presented to the user. During calibration a problem with the load cell data was observed.

Compression Fixture and Optical Microscope Integration

The compression stage was mounted and integrated with the Leica microscope so in-situ Raman spectroscopy experiments could be performed (Figure 57). After mounting the stage, the optical microscope's focusing adjustment was used to keep the ceramic sample in focus.
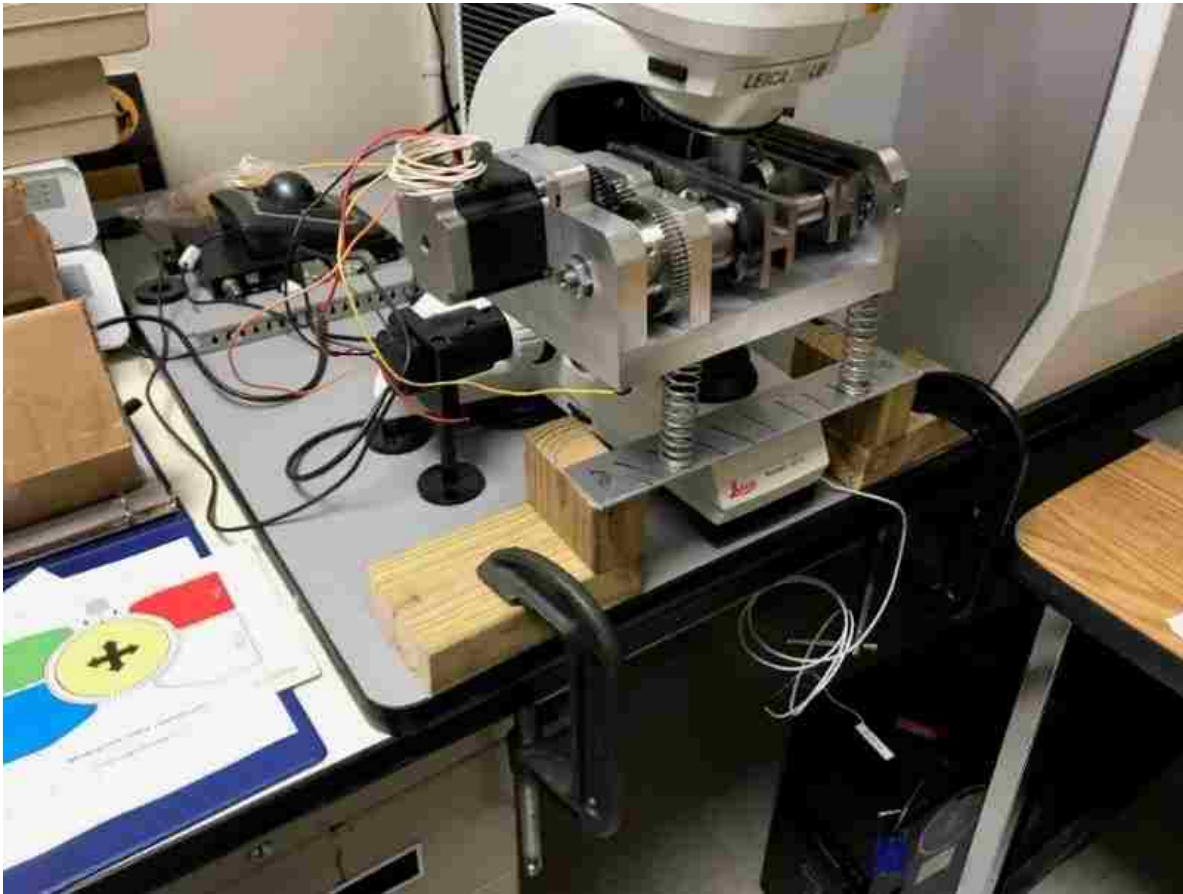
Figure 58: The mounting of the in-situ compression stage to the Leica microscope.

After mounting the stage, it was realized the spring system which reduces the weight translating it into the microscope needed to be updated to make it easier to use. Springs with a lower spring constant were chosen and the mounting plate was updated to include spring seats shown in figure 58.

Figure 59: Updated Spring system.

CHAPTER 6: PROCEDURES

This section provides an overview of the procedure used to attach the compression stage, turn on the Raman spectroscopy machine, perform a health check of the Raman spectroscopy machine, and the experimental procedure which is used to check the functionality of the compression stage. An in-depth procedure for using the compression stage has been added to the waterproof case which houses the compression stage and instrumentation when it is not in use (Figure 59).

Figure 60: Compression stage waterproof case.

Compression Fixture Setup

Attaching the compression stage to the Leica optical microscope requires removal of the any attachments which were attached to the microscope. Then, attachment of the compression stage mounting fixture, and assembly of the compression stage weight elevation system can be performed. First, the two-axis mapping stage, which is typically connected to the Leica Microscope must be removed (figure 60-part A). Next, the compression stages mounting fixture must be mounted to the Leica microscope (figure 60-part B). Then, the compression weight elevations system which uses springs must be mounted to the table (figure 60-part C). After these steps are performed, the compression stage can be attached to the mounting fixture and the four springs can be placed under the compression stage. Last, the compression stage should be aligned so the focusing point of the microscope is located on the top of the sample. Finally, the mounting fixture set screws should be tightened.

Figure 61: Compression stage setup. A) two-axis mapping stage, B) mounting fixture, C) elevations system.

Raman Spectrometer Operations

Before performing Raman spectrum acquisitions, the Raman spectrometer and optical microscope must be turned on by power on the switches in the following order. Turn on the switch 1 which provides the main power to the Raman spectroscopy machine. Next, turn on the switch 2 and turn the key to the on position. These switches provide power to the laser source. Last, turn on the microscopes light sources using switch 4. If only the optical microscope is going to be used, its lights source can be turned on individually. Also, the software which control the machine Raman spectrometer, Wire version 3.4, must be started. When powering down the machine and instrumentation, the reverse order should be performed.

Figure 62: Raman spectrograph machine power on procedure.

Raman Spectrometer Calibration

Calibration of the Raman spectroscopy system must be performed before any measurements could be done on the machine. The calibration procedure is well established and requires removal of the compression stage and mounting the calibration stage with the silicon calibration standard used for calibration. To do so, the rotation of the microscope objective lenses is required away from the measurement zone so it cannot be damaged while removing the compression fixture and installing

the calibration stage (figure 60 A). It is necessary to ensure that the stage is at the lowest position

and, then the removal of the weight elevation springs under the compression stage is required.

Figure 63: Microscope lens in rear position and removing stage support springs.

Figure 64: Calibration sample stage and calibration reference sample.

After spring removal, the mounting fixture set screws can be loosened and the compression stage can be taken out. Then, calibration stage needs to be attached and the SI standard needs to be placed (figure 63).

Using this setup, a health check of the system can be performed and if needed a further system calibration can be performed. First, a health check should be performed (figure 60 left) using the Renishaw Si standard and the acquisition should show an Si band position at 520.3 cm^{-1}. If the Si band position is off, quick calibration must be performed.
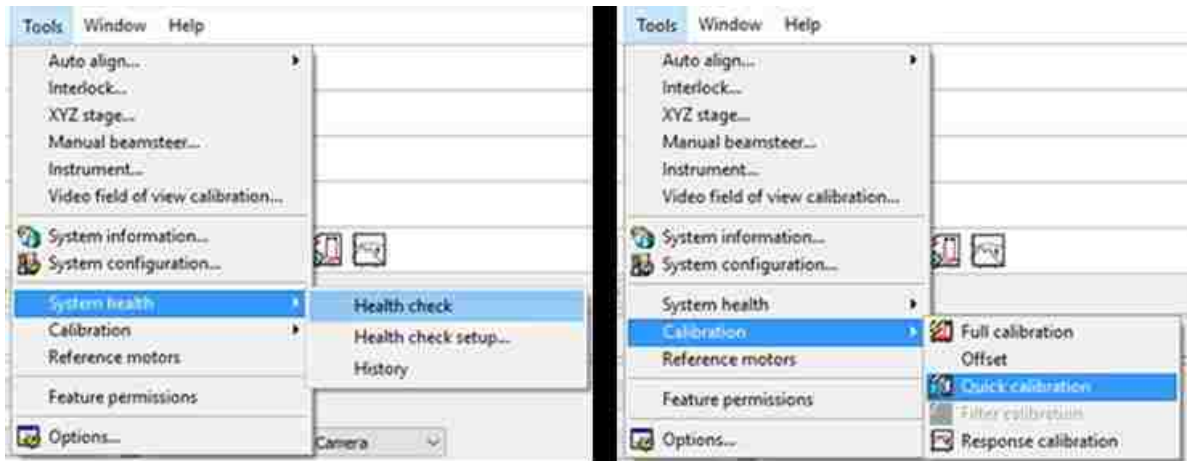
Figure 65: System health check (left) and quick calibration (left).

For experimental records, the calibration procedure results should be recorded (figure 69). Finally, reconnect the compression stage by reversing the procedure used to remove the microscope stage.

Experimental Procedure

The compression fixture, optical microscope, and micro-Raman spectrometer was used to conduct experiments and collect the Raman spectrum of $LaCoO_3$ samples. First, the $LaCoO_3$ cylindrical sample must be placed between the load and support platens. This was performed using clean medical grade specimen tweezers which allowed the sample to be properly was aligned and minimize eccentric loading. After the sample was positioned, a small preload was applied using the LabVIEW. Next, the optical microscope was used to ensure the sample and compression fixture are aligned so the sample can be focused. After the stage was setup, the Raman spectrum at increasing loads was recorded.

Figure 66: Raman experiment.

For each acquisition, the following steps were conducted prior to the acquisition. First, the average load cell voltage, load, and calculated stress were recorded from the front panel of the LabVIEW program. Next, the Leica optical microscope was focused, and an optical micrograph was recorded using the Renishaw CCD Camera. Then, the spectrum acquisition parameters were entered including the spectral acquisition range, exposure time, and data recording location on the computer. This was achieved by selecting "take a new spectral acquisition" and filing out the appropriate tabs in the dialog box. The spectral range of the acquisition was from 50-1000 Raman shift/cm^{-1} and an exposure time of 300 seconds was selected. The other parameter was set to the default settings for all acquisitions. The last step included switching the microscope from the optical setting to the spectrograph and focusing the laser. Prior to taking the spectral acquisition all lights were turned off in the room and the computer screens were set to the lowest setting to avoid altering the experimental data. Finally, to run the experiment, the run command on the wire 3.4 interface was initialed. After the spectral acquisition was complete the data recorded was saved as a .txt file in the appropriate location so it could be analyzed using Excel after testing.

CHAPTER 7: RESULTS AND DISCUSSION

Initial testing was performed on weakly Raman active $LaCoO_3$ perovskite samples machined to an average diameter of 6.04mm. Samples were tested to perform a functionality check of the compression fixture. During testing, the compression fixtures demonstrated the ability to apply a specified load while simultaneously performing structural characterization. The Raman spectroscopy setup used during the testing included a 532 nm solid Si laser to excite the sample and a single spectrograph fitted with holographic notch filters. A laser power of 25 mW was used for all spectral acquisitions. The compression fixture was mounted to the Leica optical microscope which is optically coupled to the spectrograph. During the experiment the incident and scattered beams were focused with a long working distance 50x Leica objective. Renishaw Wire software was used to setup the spectral acquisition as described in the procedure section. The collection time for a single spectrum was 300 seconds and the spectrums were recorded from 50 to 1000 Raman shift/cm^{-1}.

Four spectrum acquisitions of pure LaCoO3 perovskite cylindrical sample were used to verify the functionality of the miniature compression fixture. Each of the spectrum acquisitions was performed at an increasingly higher load. The sample was placed between the platens using clean medical grade specimen tweezers and properly was aligned to minimize eccentric loading. The first spectrum acquisition was performed after loading the sample to approximately 21 MPa. Another spectrum acquisition was performed when the sample was loaded to approximately 72 MPa. The third spectrum acquisition was performed at approximately 178 MPa. The final spectrum acquisition was performed at approximately 188 MPa.

Raman Spectrometer Calibration Results

Before collecting measurements, a heath check was performed on the spectrometer with a Renishaw Si standard which is expected to exhibit an Si band position at 520.3 cm^{-1}. The position of the Si band was at 520.5 cm^{-1} which demonstrates the spectrometer was calibrated within acceptable limits. It is important to note during testing the laser was not perfectly aligned with the crosshead in the optical micrograph. This misalignment of the system was likely caused while mounting the compression stage. Therefore, the results presented will need to be re-tested to validate their validity after the system in re-aligned.
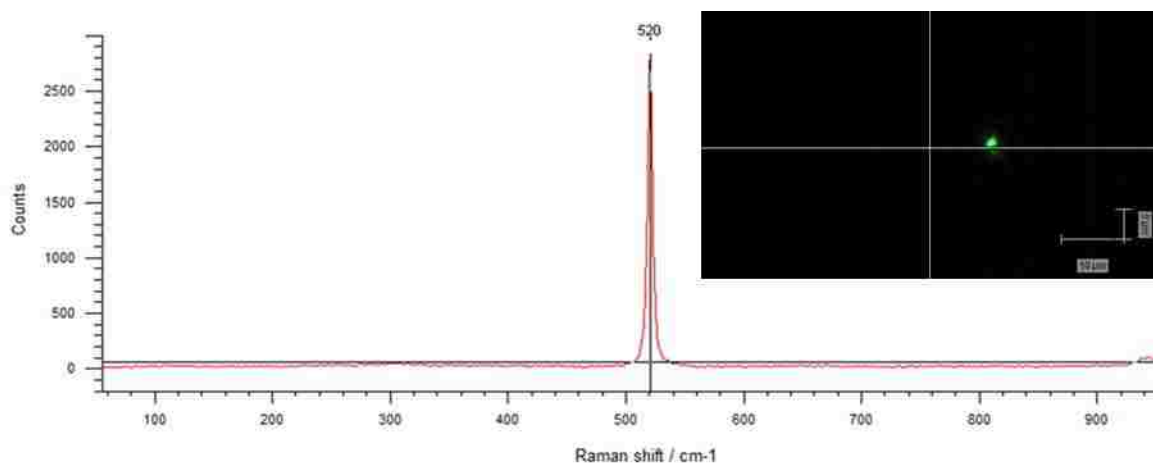
Figure 67: Raman spectra of Renishaw Si standard and Laser alignment.

Changes in Focus Location

During loading the location of the laser spot on the LaCoO$_3$ surface changed due to sample deformation, which might be a good way to measure the strain of the sample during loading. It is possible both axial and lateral strains could be detected and evaluated during future testing using optical microscopy. In this case, the deformation was tracked by identifying a unique feature on

the sample and locating it at different stress levels during loading, which is a standard digital image correlation technique used for strain measurements.

Table 4: Change in stain vs. change is stress.

	Δ **Strain**	Δ **Stress**
1-2	8μm	18.1 MPa
2-3	18μm	31.9 MPa
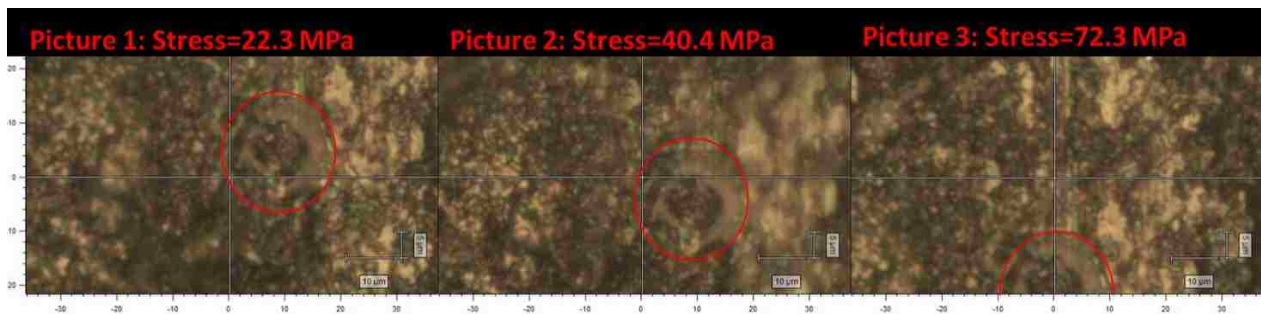
Figure 68: Changes in sample focus location due to sample deflection.

Fine adjustment in the X and Y directions would be required to perform Raman spectrum sampling in the same location because of the strain the sample experiences during loading.

Raman Spectroscopy Analysis of LaCoO$_3$

Multiple attempts were required during the first test to dial in the system. After reviewing the results of the first attempt, it appeared the laser lost focus during the experiment. It was originally alleged the laser focus issue was due to the stepper motor remaining on during the experiment. During the second attempted, the motor was shut down and the exposer time was reduced to 30s

to quickly troubleshoot the issue, but because the motor was turned so was the motors locking feature and the stress reduced to ~5 MPa. During the third test, the stress increased during testing. This was attributed to heating of the system cause by the stepper motor and it was assumed all tests would exhibit this behavior, therefore, the test was not repeated. Rather, the test should have been performed after the system reached a steady operating temperature because this problem was not experienced in other test likely because the fixture reached steady state.

As described in the procedure an optical micrograph of the sample was recorded prior to each test. Then the laser was focused, and a spectrum was collected at a preload of 21 MPa. During this test, after acquiring the spectral acquisition the applied stress increased to 26 MPa. The root cause of this increase in stress was attributed to heating of the drive system caused by the stepper motor. In this first test, optical micrographs were collected before and after the spectra collection to ensure the intensity of the laser was not damaging the sample.
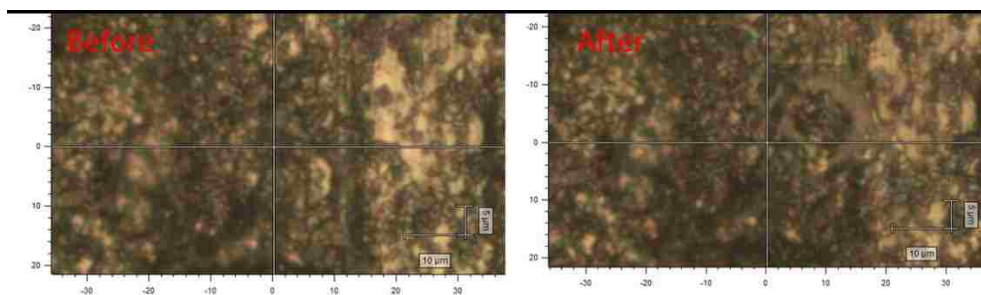
Figure 69: Optical micrographs before and after testing.

As seen in the results, the Raman active peaks of $LaCoO_3$ are weak and not easily distinguishable from the background. Pure $LaCoO_3$ Raman scattering response is a function of laser power and as the intensity of the laser in increased, two bands at 557 and 673 cm^{-1} are decrease and can be

indistinguishable [7]. In this case, shallow yet distinguishable bands belonging to the cobaltite structure were observed at 163 cm^{-1}, 435 cm-1, 574 cm^{-1}, and 675 cm^{-1}.
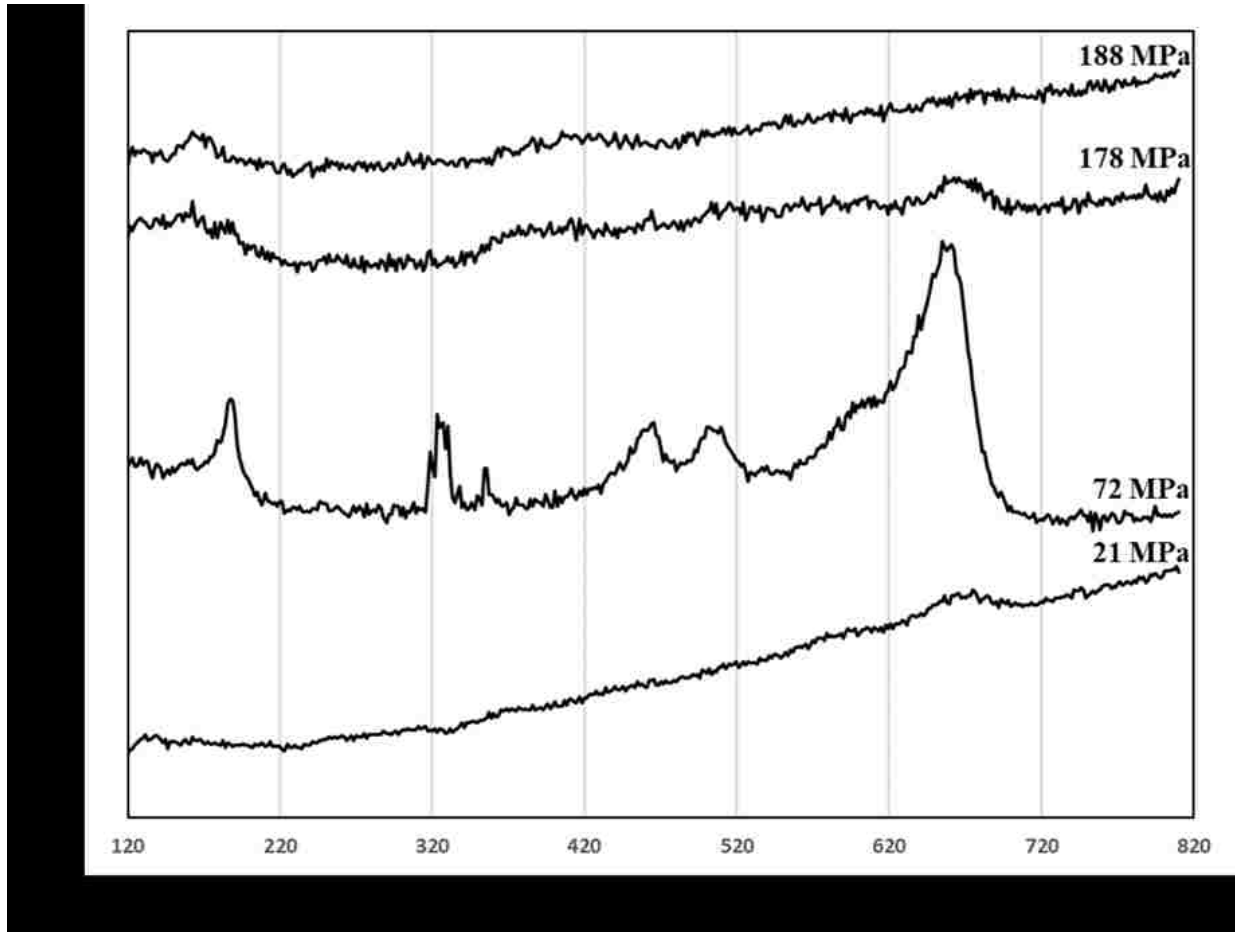
Figure 70: Raw data of LaCoO3 Raman testing.

A second vibrational spectra were taken after loading the sample to 72 MPa. It was discovered at this point that the spectrum collection location would move due to strain which is discussed in greater detail in the change in focus location section. Although the laser power was not adjusted, Raman bands became more distinguishable at this new sample location. Other bands which are not documented in other literature are present. This could be due to other materials being present at

this location and more testing will need to be performed to determine the validity of these bands. Four bands belonging to the Raman structure were observed at 163 cm^{-1}, 463 cm^{-1}, 597 cm^{-1}, and 662 cm^{-1}. Also, two bands at 325 cm^{-1} and 377 cm^{-1} are observed which will needs to be studied in more detail. A third Raman spectrum was collected to determine the Raman scattering response at 178 MPa. The intensity of cobaltite bands acquired during this test were minimal which is expected as compression strain increased and alters the crystalline structure of the materials. Bands belonging to the cobaltite structure at 463 cm^{-1}, 597 cm^{-1}, and 662 cm^{-1} are slightly visible. Also, an additional peak at 187 cm^{-1} was observed. The fourth Raman spectrum was performed at a calculated stress of 188 MPa. The intensity of Raman band at higher wave numbers reduce to insignificant levels yet the lowest band belonging to the cobaltite structure is visible at 162 cm^{-1} and 471 cm^{-1}.
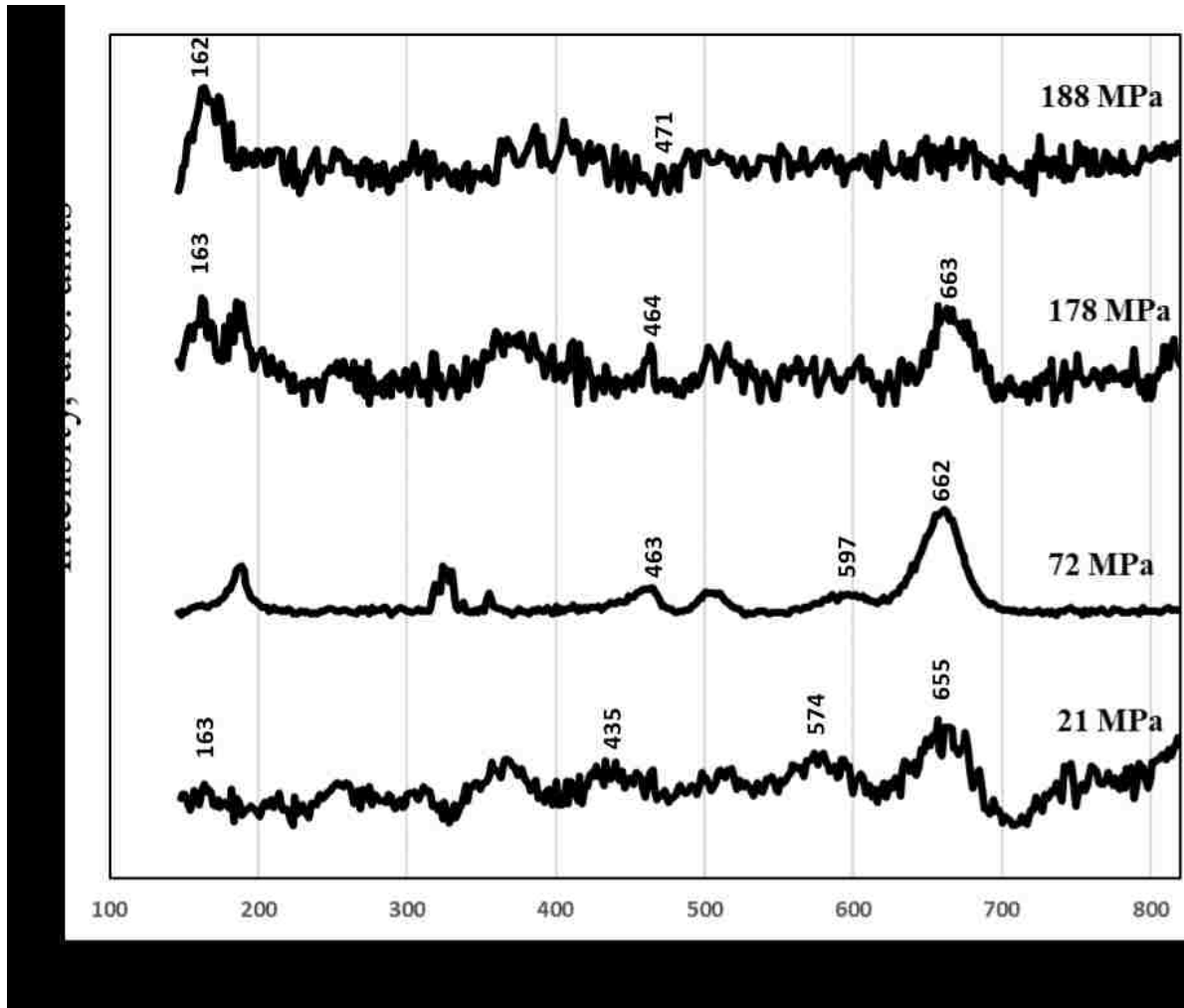
Figure 71: LaCoO$_3$ Raman Peaks at increasing compressive stress.

The Raman peaks of the material exhibited changes which resemble that of other literature. As increasing external loads were applied to the LaCoO$_3$ Perovskite, the band position tended to shift to higher wavenumbers. This effect on the vibrational response is due to the change in strain on the material's molecular latus. When Raman peaks in compression are compare to the Raman peaks in tension from 450 to 800 wave number the shift of Raman peaks in appearance due to compressive and tensile force.
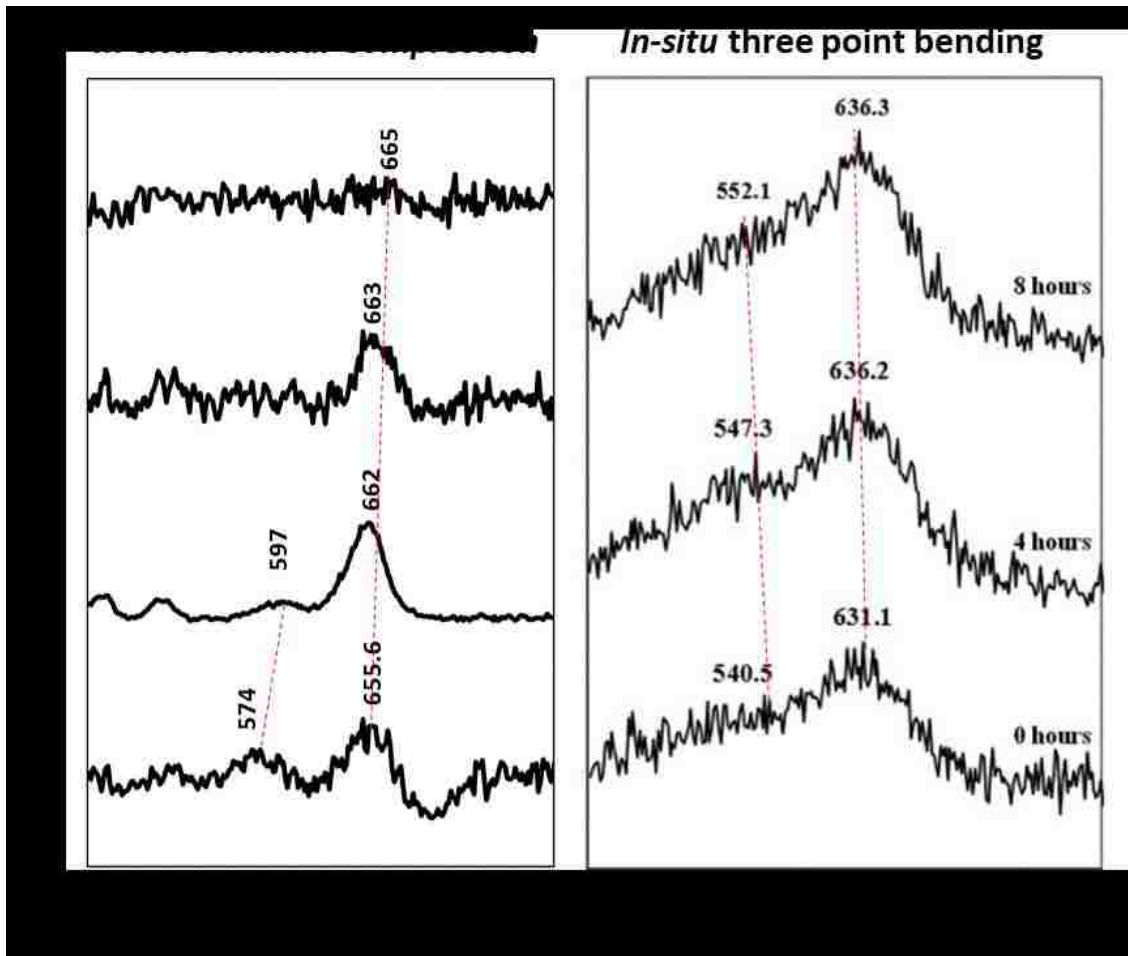
Figure 72: LaCoO$_3$ Peaks shift due to uniaxial compression and three point bending tensile

forces [23].

Also, as shown in the literature review, the Raman peaks of higher wave number became less apparent as compressive strain increase. The testing results obtained by performing four Raman spectrum acquisitions validated the ability of the compression fixture to be mounted and optically coupled to the spectrograph and study the vibrational properties of ceramics materials. The results shown in the previous section are for validating the design of the compression stage only. Additional testing will be requiring validating the vibrational response of LaCoO$_3$.

CHAPTER 8: CONCLUSIONS

A miniature compression fixture was design and assembled which allows the vibrational properties of ceramics to be tested while applying uniaxial compressive loads. The compression fixture was redesigned, and critical calculations were performed to insure design criteria would be satisfied. Also, finite element analysis was performed on the load and support crosshead to ensure margins of safety were maintained. While working with experienced machinist at the UCF machine shop, the stage was fabricated and assembled. Testing and integration demonstrated the compression fixtures ability to load ceramic samples and meet the required design criteria. Actual experiments were performed by attaching the fixture to the optical microscope and successful Raman scattering responses were recorded at four loads. These experiments showed a pattern between peak position and the external compressive force applied. Few testing techniques allow for non-destructive characterization of ceramics. The research performed in this thesis could be used in the future to determine residual stresses in ceramic materials and provide a basis for designing NDI techniques which could determine the health and status of ceramic component.

CHAPTER 9: FUTURE WORK

The future work associated with this thesis can be separated into two sections. First, future compression stage improvement and second, future testing and experiments. Future work on the compression stage will be performed to improve its performance and accuracy. The ability to change the focus location by moving the stage in the X and Y directions could be designed to allow Raman spectral acquisitions to be performed in the same location. The load cell noise issue will need to be resolved to increase the accuracy of load cell measurements and allow future system logic to be possible. A closed loop PID controller will be designed using LabVIEW which will simplify testing and reduce the chances of human error. Also, future testing and experiments will be performed to determine the Raman scattering response as a function of external load. This will include adjusting Raman spectrum parameters to achieve the best possible results. Also, the same types of testing will be performed on multiple other ceramics and ceramic compositions to be understand the structural response caused by mechanical loading.

LIST OF REFERENCES

[1] Renishaw, "A basic overview of Raman spectroscopy," 2019. [Online]. Available: https://www.renishaw.com/en/a-basic-overview-of-raman-spectroscopy--25805. [Accessed 2019 10 2].

[2] H. Kishimoto, N. Sakai, T. Horita, K. Yamaji, Y. P. Xiong, M. E. Brito and H. Yokokawa, "Rapid Phase Transformation of Zirconia, in the Ni-SeS Z Current Anode under Reducing Conditions," *Solid State Ionics,* no. 179, pp. 2037-2041, 2008.

[3] R. Stadelmann, B. Hughes and N. Orlovskaya, "Guideline of mapping parameters for Raman mapping of ZrB2-SiC ceramic composites.," *Advances in Applied Ceramics: Structural, Functional & Bioceramics,* vol. 115, no. 1, p. 21–28, 2016.

[4] K. Kleveland, N. Orlovskaya, T. Grande, A. M. Mardal Moe and M.-A. Einarsrud, "Ferroelastic Behavior of LaCoO3-Based Ceramics," *Journal of the American Ceramic Society,* vol. 84, no. 9, pp. 2029-2033, 2001.

[5] N. Russo, S. Furfori, D. Fino, G. Saracco and V. Specchia, "Lanthanum cobaltite catalysts for diesel soot combustion," *Applied Catalysis B: Environmental,* vol. 83, no. 1-2, pp. 85-95, 2008.

[6]   A. Petric, P. Huang and F. Tietz, "Evaluation of La–Sr–Co–Fe–O perovskites for solid oxide fuel cells and gas separation membranes," *Solid State Ionics,* vol. 135, no. 1-4, pp. 719-725, 2000.

[7]   N. Orlovskaya, D. Steinmetz, S. Yarmolenko, D. Pai, J. Sankar and J. Goodenough, "Detection of Temperature- and Stress-Induced Modifications of LaCoO3 by Micro-Raman Spectroscopy," *Physical Review B,* vol. 72, no. 1, pp. 2-7, 2005.

[8]   K. Matsui, H. Yoshida and Y. Ikuhara, "Grain-boundary structure and microstructure development mechanism in 2–8 mol% yttria-stabilized zirconia polycrystals," *Acta Materialia,* vol. 56, no. 6, pp. 1315-1325, 2008.

[9]   A. Ghosh, A. K. Suri, M. Pandey, S. Thomas, T. R. Rama Mohan and B. T. Rao, "Nanocrystalline zirconia-yttria system–a Raman study," *Materials Letters,* vol. 60, no. 9-10, pp. 1170-1173, 2006.

[10] F. Thévenot, "Boron carbide—A comprehensive review," *Journal of the European Ceramic Society,* vol. 6, no. 4, pp. 205-225, 1990.

[11] W. K. Barney, G. A. Sehmel and W. E. Seymour, "The Use of Boron Carbide for Reactor Control," *Nuclear Science and Engineering,* vol. 4, no. 3, pp. 439-448, 1958.

[12] P. Jannotti, G. Subhash, J. Q. Zheng, V. Halls, P. G. Karandikar, S. Salamone and M. K. Aghajanian, "Raman spectroscopic characterization of the core-rim structure in

reaction bonded boron carbide ceramics," *Applied Physics Letters,* vol. 106, no. 4, 2015.

[13] W. Chong-Min, P. Xiaoqing, F. L. Riley and M. Mitomo, "Silicon nitride crystal structure and observations of lattice defects," *Journal of Material Science,* vol. 31, no. 20, pp. 5281-5298, 1996.

[14] "Silicon Nitride (Si3N4) Properties and Applications," AZO Materials, 6 February 2001. [Online]. Available: https://www.azom.com/article.aspx?ArticleID=53. [Accessed 5 August 2019].

[15] A. J. Eckel, "Silicon nitride rocket thrusters test fired successfully.," in *NASA Glenn Research Centre press release*, 2000.

[16] J. Z. Jiang, K. St˚ahl, R. W. Berg, D. J. Frost and T. J. Zhou, "Structural characterization of cubic silicon nitride," *Europhysics Letters,* vol. 51, no. 1, p. 62067, 2000.

[17] V. A. Izhevskyi, L. A. Genova, J. C. Bressiani and A. H. Bressiani, "Review article: Silicon Carbide. Structure, Properties and Processing," *Cerâmica,* vol. 46, no. 297, 2000.

[18] L. Vargas-Gonzalez and R. F. Speyer, "Flexural Strength, Fracture Toughness, and Hardness of Silicon Carbide and Boron Carbide Armor Ceramics," *Applied Ceramic Technology,* vol. 7, no. 6, pp. 643-651, 2010.

[19] M. Albano, R. B. Morles and M. Marchetti, "Coating effects on thermal properties of carbon carbon and carbon silicon carbide composites for space thermal protection systems," *Acta Astronautica,* vol. 99, pp. 276-282, 2014.

[20] P. Borowicz, T. Gutt and T. Malachowski, "Structural investigation of silicon carbide with micro-Raman spectroscopy," in *Mixed Design of Integrated Circuits and Systems (MIXDES)*, Bydgoszcz, 2009.

[21] J. Nowak and Z. Shan, "In-Situ Compression of Nanopillars," *Hysitron,* 2017.

[22] "Hysitron PI 95," Bruker, 2019. [Online]. Available: https://www.bruker.com/products/surface-and-dimensional-analysis/nanomechanical-test-instruments/nanomechanical-test-instruments-for-microscopes/pi-95-tem-picoindenter/overview.html. [Accessed 2 October 2019].

[23] N. Fist, J. Dinan, R. Stadelmann and N. Orlovskaya, "In situ three point bending device for measurements of vibrational response of ceramics under stress by microRaman spectroscopy," *Advances in Applied Ceramics: Structural, Functional and Bioceramics,* vol. 111, no. 7, pp. 433-439, 2012.

[24] S. Romeis, J. Paul, M. Ziener and W. Peukert, "A novel apparatus for in situ compression of submicron structures and particles in a high resolution SEM," *Review of Scientific Instruments,* vol. 83, no. 9, 2012.

[25] E. K. Moo, S. K. Han, S. Federico, S. C. Sibole, A. Jinha, N. A. A. Osman, B. Pingguan-Murphy and W. Herzog, "Extracellular matrix integrity affects the mechanical behaviour of in-situ chondrocytes under compression," *Journal of Biomechanics,* vol. 47, no. 5, pp. 1004-1013, 2014.

[26] G. D. Dutel, P. Langlois, D. Tingaud and G. Dirras, "Room-temperature deformation micro-mechanisms of polycrystalline nickel processed by spark plasma sintering," *Material Characterization,* vol. 79, pp. 76-83, 2013.

[27] I. Hanhan, E. Durnberg, g. Freihofer, P. Akin and S. Raghavan, "Portable Piezospectroscopy system: non-contact in-situ stress sensing through high resolution photo-luminescent mapping," *Journal of Instrumentation,* vol. 9, 2014.

[28] G. Freihofer, L. Poliah, K. Walker, A. Medina and S. Raghavan, "Optical stress probe: in-situ stress mapping with Raman and Photo-stimulated luminescence spectroscopy," *Journal of Instrumentation,* vol. 5, 2010.

[29] "Tensile Testing up to 10kN," Kammrath Weiss Gmbh, 2015. [Online]. Available: https://www.kammrath-weiss.com/en/products/materials/tensile-compression.html. [Accessed 21 May 2019].

[30] "MTII/ Fullam SEM Tester Series," MTI Instruments, 2017. [Online]. Available:

https://www.mtiinstruments.com/wp-content/uploads/2017/08/Tensile-Stage.pdf.

[Accessed 17 2019 July].

[31] "200N compression & horizontal bending stage," Deben, 2018. [Online]. Available:

https://deben.co.uk/tensile-testing/xrd/mini-tensile-tester-200n-compression-

horizontal-bending-stage/. [Accessed 15 June 2019].

[32] D. Goran, "Orientation contrast imaging and EBSD," Bruker Nano GmbH, Berlin, 2015.

[33] "Thomson Linear Motion Systems," Thomson, 2019. [Online]. Available:

www.thompsonlinear.com/linear/motion. [Accessed 6 October 2019].

[34] "How a Ball Screw Works," Barnes Industries, Inc., 2018. [Online]. Available:

http://www.barnesballscrew.com/how-a-ball-screw-works/. [Accessed 15 October

2019].

[35] "Spur Gear Tooth Component Identification," Engineers Edge, 2019. [Online]. Available:

https://www.engineersedge.com/gears/gear_tooth_parts.htm. [Accessed 15 October

2019].

[36] "Standard Specification for Stainless Steel Bars and Shapes," *ASTM,* Vols. A276/A276M-

17, 2017.

[37] "Stainless Steel – Grade 440C (UNS S44004)," AZO Materials, 2019. [Online]. Available: https://www.azom.com/article.aspx?ArticleID=6846. [Accessed 28 June 2019].

[38] S. Online, "User's Manual for MA860H High Performance Microstepping Driver".